


# Ram-air cooling for fuel cell aircraft

Downloaded from: https://research.chalmers.se, 2026-11-05 00:28 UTC

Citation for the original published paper (version of record):
Svensson, C., Miltén, P., Grönstedt, T. (2027). Ram-air cooling for fuel cell aircraft. Aerospace Science and Technology, 180. http://dx.doi.org/10.1016/j.ast.2026.114103

N.B. When citing this work, cite the original published paper.

research.chalmers.se offers the possibility of retrieving research publications produced at Chalmers University of Technology. It covers all kind of research output: articles, dissertations, conference papers, reports etc. since 2004. research.chalmers.se is administrated and maintained by Chalmers Library

(article starts on next page)

Aerospace Science and Technology 180 (2027) 114103

Contents lists available at ScienceDirect

Aerospace Science and Technology

journal homepage: www.elsevier.com/locate/aescte

# Ram-air cooling for fuel cell aircraft

Christian Svensson*, Petter Miltén, Tomas Grönstedt

*Division of Fluid Dynamics, Department of Mechanical Engineering, Chalmers University of Technology, Gothenburg, 412 96, Sweden*

ARTICLE INFO

Communicated by Kontis Konstantinos

*Keywords:*
Ducted heat exchanger
Ram-air
Meredith effect
Fuel cell aircraft
Low-drag cooling
Thermal management

ABSTRACT

The ram-air cooling system for a fuel cell aircraft is conceptually designed. The ducted heat exchanger model captures internal and external flow effects, fan and pump operation and nozzle variability. Certain aerodynamic aspects are validated using RANS CFD. The complete system is optimized for minimal parasitic power draw. For an ATR 72-sized aircraft, an optimal design only capable of cruise requires approximately 4.3 % of the expected 1.2 MW fuel cell stack output. Enabling ISA +25 °C hot-day take-off requires a larger system, increasing the power draw during cruise to 11.3 % of the stack output. The take-off requires 15.2 % of the expected 2 MW stack output. The results demonstrate that ram-air cooling remains feasible with low-temperature fuel cells, although take-off requirements impose a substantial cruise penalty. Three key enablers to low drag are identified: inlet oversizing, an application-suited heat exchanger design and an upstream-mounted fan.

## 1. Introduction

The need for megawatt-level heat rejection in fuel cell aircraft poses a real challenge, as the weight and aerodynamic drag of the system risk to negate any efficiency benefits brought on by the fuel cell system. Fuel cell powered alternatives to regional turboprop aircraft such as the ATR 72 or De Havilland Dash-8 would require fuel cell systems capable of providing megawatt-class electric power [1,2].

A reasonable estimate for the cell efficiency in a modern proton-exchange membrane fuel cell (PEMFC) is around 50 % for low to high temperature PEMFCs (LT-PEMFC, HT-PEMFC) [3]. With this efficiency, 1 MW of power output will require 1 MW of heat rejection. Because of the low rate of heat rejection in the fuel cell's reactant streams, most of the generated heat has to be removed via dedicated cooling systems, such as a liquid-to-air heat exchanger (HEX) [4]. In such a setup, a coolant liquid is circulated through each individual fuel cell, where it absorbs heat and increases in temperature. It then passes through a heat exchanger, where the coolant rejects heat into the airstream. The heat exchanger is then ideally housed within a cooling duct in order to maximize the cooling effect from the airstream and minimize the drag.

The topic of ducted heat exchangers in aircraft has been extensively studied in the past. During the 1930s and 1940s, it was of great interest to minimize the drag caused by the liquid-to-air heat exchangers used for cooling military aircraft piston engines. The aerothermal phenomena of reducing internal drag (or even producing thrust) by compressing, heating and expanding the cooling airstream in a carefully designed duct was described in a paper from 1935 by F.W. Meredith [5]. This now well-known *Meredith effect* was used with great success in some of the fighter aircraft of that era. The cooling needs of aircraft engines have since then dropped with the introduction of gas-turbines [6], and ducted heat exchanger research has then shifted focus towards aircraft climate control systems and other systems with much lower heat rejection needs. With the advent of fuel cell electric aircraft, research into low-drag ducted heat exchangers has again become a research area of great interest.

Rejecting a megawatt of heat to the surrounding at a small performance penalty is difficult. This is because the cooling system imposes both internal and external aerodynamic drag and requires direct power to drive electric components such as coolant pumps and fans. In addition to this, the system needs to perform well under varying operating conditions and provide optimum performance with respect to the aircraft mission. On one hand, the take-off requires a high amount of heat rejection in unfavorable ambient conditions, as the temperature is high and the airspeed low. On the other hand, in cruise the airspeed and ambient temperature are favorable. As the aircraft will spend most time in cruise conditions, and because of the high airspeed, it is vital to minimize the drag in these conditions. However, minimizing cruise drag involves downsizing the system, which in turn will impact the take-off performance. A very small cooling duct will do well in cruise, but needs a powerful fan in take-off, which leads to a weight penalty carried in cruise. As will be outlined in this work, these conflicting requirements are what drive the design.

Several recent studies have investigated low-drag cooling systems for electric and fuel cell electric aircraft [7–16]. WIEGAND et al. [17] studied various types of hybrid-electric aircraft and optimized the

* Corresponding author.
*E-mail addresses:* chrissv@chalmers.se (C. Svensson), milten@chalmers.se (P. Miltén), tomas.gronstedt@chalmers.se (T. Grönstedt).

https://doi.org/10.1016/j.ast.2026.114103
Received 30 July 2026; Received in revised form 10 September 2026; Accepted 28 September 2026
Available online 20 October 2026
1270-9638/© 2026 The Author(s). Published by Elsevier Masson SAS. This is an open access article under the CC BY license (http://creativecommons.org/licenses/by/4.0/).

design of their respective thermal management systems for minimal climate impact. A fully electric ATR 72 was studied in both a LT-PEMFC and HT-PEMFC configuration. The cooling system consisted of a ducted heat exchanger, an electric fan mounted upstream of the heat exchanger and a coolant pump. The heat rejection rate was equal to the waste heat produced. Only the high-temperature PEMFC was feasible in a full-electric configuration, while both low and high temperature PEMFCs could be used in a turboprop-hybrid configuration. Frey et al. [18] investigated a ducted heat exchanger with a fan located upstream. The cooling requirement was set to 1 MW to reflect a Dash-8 fuel cell propulsion unit with a 50 % efficiency. A heat exchanger effectiveness of 0.95 was targeted and the fan had to be deployed to cancel out the internal drag and produce thrust. The fan was placed upstream of the heat exchanger as locating it downstream would not provide any compression before the heat addition. The choice of liquid coolant has also been investigated by Frey et al. [19], where the optimal liquid was found to be a hydrocarbon based liquid coolant. Armbrüster et al. [20] investigated the performance of several heat exchanger and fan configurations for an ATR 72-like aircraft. The heat exchanger flow configurations tried were parallel, counter, cross, parallel-cross and counter-cross flow. Each heat exchanger was then combined with a duct and a upstream or downstream mounted fan. The counter-cross flow heat exchanger was shown to provide the best effectiveness and compactness. It was also demonstrated that an upstream mounted fan negatively impacted heat exchanger performance due to the temperature rise caused by the compression. Adler et al. [21] performed a design optimization study on a duct using CFD coupled to a heat exchanger model. An axi-symmetric and a superelliptical duct geometry were parametrized and then shape optimized in order to minimize an overall power draw in a multi-point simulation consisting of a take-off, cruise and a high-speed cruise. Overall, the optimization tended to designs with short inlet sections and a general trend of oversizing the inlet area in order to clear the take-off constraint was observed. Kellerman et al. [22] investigated a ducted heat exchanger cooling system for a 180 PAX hybrid-electric aircraft. The required heat rejection was smaller compared to the previously mentioned studies, with the design point having the highest requirement at 83.6 kW. The cooling duct was made up of a diffuser section followed by a heat exchanger, fan and a nozzle. The design was able to clear the take-off constraint using the fan, or alternatively the take-off cooling requirement could be managed by oversizing the inlet.

Due to the conflicting requirements imposed by the take-off and cruise conditions, a comprehensive system design study is performed in order to quantify the fundamental aerodynamic and thermodynamic mechanisms of the design problem and to establish the resulting system-level design trades. To achieve this, we develop a quasi-1D ducted heat exchanger code that is capable of capturing all relevant physical mechanisms such as duct and heat exchanger pressure loss, external streamtube diffusion, spillage drag, fan operation and nozzle variability. A RANS CFD study is performed in order to validate the quasi-1D method. The ducted heat exchanger code is then used to simultaneously optimize the design of the duct, heat exchanger, fan and coolant pump for minimal parasitic power draw in representative operating conditions. The aerothermal result and system cost of the optimal design are then presented and compared with an ideal cruise-only design. The results demonstrate that, under conservative engineering assumptions, the heat rejection needed for a low-temperature PEM fuel cell is achievable at a modest performance penalty. Establishing this quantitative result using a balanced multidisciplinary method, constitutes the main contribution from this work. Furthermore, an analysis into the different fan configurations is made, shedding new light on under which conditions different architectures become superior. Lastly, overall design recommendations are presented.

**Table 1**
Streamwise stations in the cooling duct.

| Station | Name | Area |
|---|---|---|
| $\infty$ | Freestream | $A_\infty = \mathrm{MFR} \cdot A_0$ |
| 0 | Intake face | $A_0$ |
| 1 | Diffuser inlet | $A_1 = \mathrm{AR}_i \cdot A_0$ |
| 2 | Diffuser exit | $A_2 = \mathrm{AR}_d \cdot A_1$ |
| 3 | HEX inlet | $A_3 = A_2$ |
| 4 | HEX exit | $A_4 = A_3$ |
| 5 | Nozzle inlet | $A_5 = A_4$ |
| 6 | Nozzle exit | $A_6 = \mathrm{AR}_n \cdot A_5$ |

## 2. Methodology

This section presents the key equations and calculation procedures. Further details on the cooling duct model, component mass estimation, and the fixed model parameters required to reproduce the analysis (Table A.1) are provided in Appendix A.2.

### 2.1. Fuel cell cooling need

For the fuel cell system, the rate of heat generated is a function of the total electric power $P_{\mathrm{FC}}$ produced by the stack, and its cell efficiency $\eta_{\mathrm{cell}}$ at that operating point, that is

$$\eta_{\mathrm{cell}} = \frac{P_{\mathrm{FC}}}{Q_{\mathrm{FC}} + P_{\mathrm{FC}}}$$

which gives

$$Q_{\mathrm{FC}} = \left(1/\eta_{\mathrm{cell}} - 1\right) P_{\mathrm{FC}}\,. \tag{1}$$

The total electric power generated by the fuel cell system consists of both useful propulsive power, and power generated in order to drive the auxiliary balance-of-plant (BoP) devices, such as the cooling system. The heat generated in Eq. (1) can be partially rejected by the air, hydrogen, and water mass flows, the rest being removed by the dedicated cooling system. The cooling system then has to provide a heat transfer rate equal to

$$Q = Q_{\mathrm{FC}} - Q_{\mathrm{air,\,FC}} - Q_{\mathrm{H_2}} - Q_{\mathrm{H_2O}}$$

For a PEMFC stack operating in an aircraft, a reasonable assumption is that $Q_{\mathrm{air,\,FC}} = Q_{\mathrm{H_2O}} = 0$. The first reason for this is that the stack is pressurized, which requires compression of the inlet air, increasing its temperature. The amount of cooling (if any) provided by the reactant air will therefore be very dependent on ambient conditions and the level of intercooling performed. The second reason for this is the state of the water in the exhaust. If it is at the stack temperature and in liquid form then it is only the hydrogen that can be used to remove any meaningful amount of heat.

### 2.2. Ram-air cooling

A ducted heat exchanger, as illustrated in Fig. 1, is considered. The duct consists of an inlet section upstream of the heat exchanger, and a nozzle section downstream of it. The inlet section captures the streamtube of air and slows it down inside the diffuser section which also increases the static pressure. The slow-moving air is then heated inside the heat exchanger before transitioning into the nozzle section, which accelerates the flow before it exits into the freestream again. The duct's station numbering and areas are described in Table 1.

Fig. 1 illustrates a cooling duct in cruise operation. In this condition, the freestream is cold and the dynamic pressure plentiful due to the flight speed. There is therefore an excess of freestream cooling

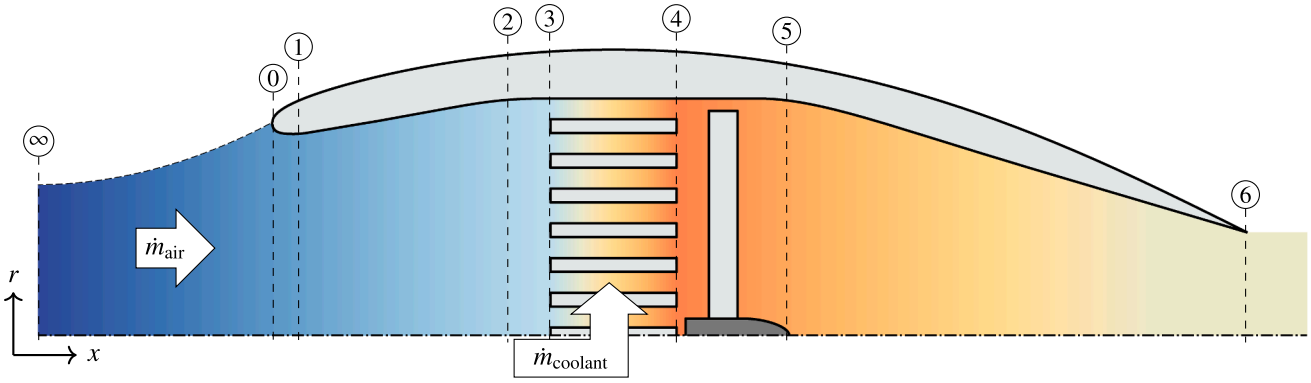



**Fig. 1.** Conceptual illustration of an axisymmetric ram-air cooling duct, with the color gradient representing the change in air static temperature. Booster fan can be located before or after the heat exchanger.

potential. The right amount of cooling is achieved by limiting the mass flow of air, which is accomplished by a convergent nozzle constricting the nozzle exit area. This constriction of mass flow has the effect of diffusing the captured streamtube upstream of the duct, again see Fig. 1. The external streamtube diffusion can, in this flight condition, be increased by oversizing the inlet area. In the take-off condition on the other hand, there may not be enough ram-pressure, and the mass flow through the cooling duct may therefore be insufficient. In this case, the total pressure through the system has to be increased with a booster fan.

### 2.3. Heat transfer rate

The rate at which the heat exchanger transfers heat from a hot to a cold fluid can be expressed in terms of an effectiveness $\epsilon$ and a theoretical maximum heat transfer rate $Q_{\max}$

$$Q = \epsilon Q_{\max} \,. \tag{2}$$

The theoretical maximum is defined as

$$Q_{\max} = C_{\min}\left(T_{0_{\mathrm{h,\,in}}} - T_{0_{\mathrm{c,\,in}}}\right) \tag{3}$$

where $T_{0_{\mathrm{h,\,in}}}$, $T_{0_{\mathrm{c,\,in}}}$ are the hot and cold inlet total temperatures, respectively, and

$$C_{\min} = \min(C_h, C_c) = \min\left(\dot{m}_{\mathrm{h}} c_{p_{\mathrm{h}}},\, \dot{m}_{\mathrm{c}} c_{p_{\mathrm{c}}}\right) \tag{4}$$

is the minimum heat capacity rate. For a liquid-to-air heat exchanger used in an aircraft, the hot-side heat capacity rate is larger than the cold side ($C_h > C_c$) and therefore the air is the limiting fluid. With this in mind, it can be seen from Eqs. (2)–(4) that the cooling provided by the ducted heat exchanger depends on its effectiveness, the hot and cold inlet temperatures and the heat capactity rate of the air stream inside the duct.

A heat exchanger with a higher effectiveness will be able to transfer more heat for a given amount of mass flow compared to a design with lower effectiveness. The cost of this increased heat transfer is an increase in frictional losses. This happens because the convective heat transfer is proportional to the shear-stress experienced at the heat exchanger surfaces [23]. In the context of the overall aircraft performance, the highest possible effectiveness may not always be desired, as the loss of total pressure and added weight will have a direct effect on the aircraft's efficiency and range.

### 2.4. Mass flow and thrust

For subsonic flow through an ideal nozzle, the exit static pressure will match that of the ambient, $p_6 = p_\infty$. The nozzle exit velocity, $v_6$, can then be expressed in terms of the local total temperature $T_{06}$ and total pressure $p_{06}$

$$v_6 = \sqrt{\left(\frac{2\gamma}{\gamma-1}\right) R T_{06}\left[1 - \left(\frac{p_\infty}{p_{06}}\right)^{\frac{\gamma-1}{\gamma}}\right]}$$

and for an isentropic expansion the mass flow and gross thrust ($F_{\mathrm{gross}} = \dot{m} v_6$) become

$$\dot{m}_{\mathrm{air}} = \frac{p_\infty A_6}{R\sqrt{T_{06}}\left(\frac{p_\infty}{p_{06}}\right)^{\frac{\gamma-1}{\gamma}}} \sqrt{\left(\frac{2\gamma}{\gamma-1}\right) R\left[1 - \left(\frac{p_\infty}{p_{06}}\right)^{\frac{\gamma-1}{\gamma}}\right]}$$

$$F_{\mathrm{gross}} = \left(\frac{2\gamma}{\gamma-1}\right) p_\infty A_6\left[\left(\frac{p_{06}}{p_\infty}\right)^{\frac{\gamma-1}{\gamma}} - 1\right]. \tag{5}$$

The ratio of total to static pressure in the ideal nozzle is known as the nozzle pressure ratio ($p_{06} \approx p_{05}$, $\mathrm{NPR} = p_{05}/p_\infty$).

From the above equations, we can identify three important coupled mechanisms in a ram-air system.

1. For an isothermal ram-air duct, the total pressure is the main driving force for the exit velocity and mass flow.
2. Increasing the total temperature will for a given NPR and exit area increase the exit velocity but decrease the mass flow rate.
3. For a given nozzle exit area, the gross thrust is completely independent of the temperature and depends only on the NPR.

In a real ram-air cooling system, the heating of the cooling air is dictated by the heat transferred from the heat exchanger, which in turn is mass flow dependent. As the total temperature rises, the mass flow drops. In order to maintain the heat transfer rate, the mass flow has to be increased by opening the nozzle exit area until the cooling requirement is met. The Meredith effect is then a phenomenon best observed in the uninstalled net thrust equation

$$F_{\mathrm{net,\,uninst.}} = F_{\mathrm{gross}} - F_{\mathrm{ram}} = \dot{m}\left(v_6 - v_\infty\right) \tag{6}$$

whereby raising the total temperature or total pressure increases the exit velocity $v_6$. To increase the exit speed while maintaining a set level of heat transfer, the designer of a low-drag cooling system has to then balance between

(a) increasing the NPR by minimizing losses, which requires a lower heat exchanger effectiveness with a large mass flow, resulting in a decrease in total temperature, or
(b) increasing the total temperature by increasing heat exchanger effectiveness, which increases losses and decreases the mass flow, resulting in a decrease in NPR.

The loss of total pressure can be attributed to two main mechanisms, either flow-induced or due to heat addition. The first kind occurs through

viscous dissipation in the boundary layer, and through flow separation where the streamwise energy is lost to large scale mixing. The second kind of loss is a non-viscous effect which occurs when heat is added to the flow. This raises both the total temperature and the entropy of the flow (Rayleigh effect).

The total pressure in the system can be increased by using a fan. This compression of the air costs shaft power, and will in addition to this increase the total temperature of the air. Mounting the fan upstream of the heat exchanger can therefore degrade the heat exchanger temperature difference, but will on the other hand require less shaft power to achieve a given pressure rise compared to a downstream-mounted fan. As is seen in Eq. (5), for a given pressure rise, the location of the fan will not directly influence the gross thrust. It will however influence the conditions in the heat exchanger, which can affect the total pressure loss inside it and the required mass flow.

### 2.5. Cooling duct model

The performance of the cooling duct described in Section 2.2 is simulated by applying the compressible flow equations on a station-based quasi-1D geometry. The geometries considered are axisymmetric, which integrates well with axial fans and allows for the use of well-established correlation methods for external drag (see Section 2.7.1) and diffuser loss performance (see Appendix A.2). The accuracy of the model has been validated by comparing it with a commercial CFD solver, see Appendix B.

The local Mach number at a streamwise station inside the duct is solved numerically by using the continuity equation with the previous station's Mach number $M$, the area ratio AR, total pressure ratio $\pi$ and total temperature ratio $\tau$ between the two stations. The remaining flow state variables such as static pressure, static temperature, density and airspeed can then be found via total flow condition relations for a calorically perfect gas. The particular flow conditions for each station inside the duct are detailed in Appendix A.2.

A root-finding routine is used to find the air mass flow accepted by the cooling duct, which is regulated by the nozzle exit condition

$$p_6 - p_\infty = 0\,. \tag{7}$$

This solution is considered physical, but might produce excessive or inadequate cooling. Therefore, the second variable solved for is either the fan total pressure ratio ($\pi_{\text{fan}}$) or the area ratio of the nozzle ($\text{AR}_n$), so that the cooling residual is zero,

$$Q - Q_{\text{required}} = 0\,.$$

If the solver is set to *fan mode*, i.e. that $\pi_{\text{fan}}$ is solved for, then $\text{AR}_n$ can either be fixed or treated as a design variable inside an optimization (see Table 2). In *nozzle mode*, $\text{AR}_n$ is solved for and $\pi_{\text{fan}}$ is treated as a design variable. The code can also be run with only the pressure residual in Eq. (7) being solved for.

### 2.6. Heat exchanger model

The heat exchanger is assumed to have a frontal area in the airstream equal to the axisymmetric internal cooling duct cross-section. It is furthermore assumed to be of cross-flow type. The $\epsilon$ – NTU method is used to calculate the resulting heat exchanger effectiveness, which together with the inlet temperatures and fluid properties for the hot and cold side yields the resulting heat rejection rate using Eq. (2).

The framework `GenHEX` [24,25] is used in order to geometrically define a heat exchanger and estimate its thermal and hydraulic performance. In GenHEX, a geometry is defined by the overall dimensions ($L_x, L_y, L_z$) and three geometrical generalized parameters (GGPs): the void fraction ratio $\sigma_r$, the surface area density ratio $\alpha_r$ and a solidity factor $\chi$.

The void fraction ratio sets the ratio between the air and coolant streams' void fractions

$$\sigma_r = \frac{\sigma_{\text{air}}}{\sigma_{\text{coolant}}} = \frac{\left(A_{ff}/A_{fr}\right)_{\text{air}}}{\left(A_{ff}/A_{fr}\right)_{\text{coolant}}}\,,$$

where $A_{ff}$ is the free-flow area and $A_{fr}$ the frontal area (note that the frontal area is different for the two streams in a cross-flow design). In the context of the cooling duct described in Table 1, the frontal area is $A_{fr_{\text{air}}} = L_y L_z = A_3$ and the free-flow area $A_{ff_{\text{air}}} = \left(\sigma A_{fr}\right)_{\text{air}}$. A liquid-to-air heat exchanger will typically have $\sigma_r > 1$ as the heat capacity rate of the coolant is much greater than that of the air, and therefore needs less volume to flow through.

The surface area density ratio sets the ratio between the air and coolant streams' surface area densities (which simplifies to a ratio of surface areas for the two streams)

$$\alpha_r = \frac{\alpha_{\text{air}}}{\alpha_{\text{coolant}}} = \frac{A_{\text{air}}/V_t}{A_{\text{coolant}}/V_t} = \frac{A_{\text{air}}}{A_{\text{coolant}}}\,,$$

where $A_{\text{air}}, A_{\text{coolant}}$ are the total heat transfer surface areas and $V_t = L_x L_y L_z$ the total volume of the heat exchanger. This parameter has the effect of increasing the surface area in a stream by introducing fins. A heat exchanger with $\alpha_r > 1$ will have fins in the air stream, but not in the coolant stream (and vice-versa for $\alpha_r < 1$). A ratio close to unity implies no fins in either stream.

The solidity factor describes how much of the total volume is occupied by the heat exchanger walls, fins and channels. The ratio is defined as

$$\chi = \frac{V_s}{V_t}\,,$$

where $V_s$ is the solid volume.

The GGPs, overall dimensions and a wall-thickness $t_w$ are then used to define a continuous space of heat exchanger designs. Within this space, real heat exchanger designs that have been tested experimentally exist [26]. These experimental results are then used to form correlations for the friction factor $f_D$ and the Colburn factor $j$ as a function of the heat exchanger geometry. These correlations are then mapped onto the design space in order to quantify the heat transfer and hydraulic performance for every possible heat exchanger design.

### 2.7. Power draw modeling

The fundamental design problem is to meet a heat rejection requirement with the smallest amount of parasitic power, or power draw, used. The power draw originates from the extra aerodynamic drag added by the air flowing around and through the cooling duct, as well as electric components such as the coolant pump or airflow booster fan. The electric components incur a direct power draw, while the aerodynamic drag forces the aircraft to create thrust from the propellers, which draws electric power. The total power draw is

$$P_{\text{total}} = P_{\text{drag}} + P_{\text{device}}$$

where the drag-induced electric power draw $P_{\text{drag}}$ is simply the mechanical work to overcome the drag

$$P_{\text{drag}} = \frac{D_{\text{total}} v_\infty}{\eta_{\text{prop}} \eta_{\text{motor}}} \tag{8}$$

where $v_\infty$ is the freestream velocity, $\eta_{\text{prop}}$ the propulsive efficiency and $\eta_{\text{motor}}$ the efficiency of the electric motor (see Table A.1). The total drag is made up of internal, external and lift-induced drag due to added mass

$$D_{\text{total}} = D_{\text{ext}} + D_{\text{mass}} + D_{\text{int}}\,. \tag{9}$$

The external drag is due to pressure and shear forces acting on the cooling duct exterior. The drag is commonly represented as the product of a drag coefficient ($C_{\text{D}}$), dynamic pressure ($q_\infty$) and a reference area ($S_{\text{ref}}$)

$$D_{\text{ext}} = q_\infty C_{\text{D}} S_{\text{ref}}\,. \tag{10}$$

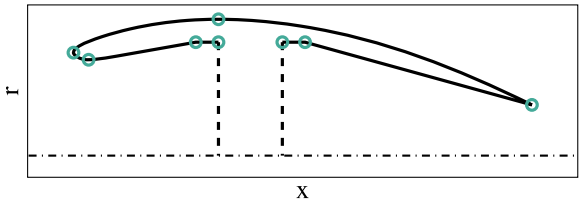



**Fig. 2.** Example geometry using the CST spline method [28]. Dashed vertical lines indicate the inlet and outlet faces of the heat exchanger. The coordinates of the geometrical stations are marked by green circles. (For interpretation of the references to color in this figure legend, the reader is referred to the web version of this article.)

Other than the geometric shape of the cooling duct, $C_D$ will vary as a function of the mass flow ratio (MFR) and freestream Mach number.

Lastly, $D_{mass}$ is the drag due to lift from the added mass of the cooling duct, heat exchanger, liquid coolant, fan (including motor) and pump

$$D_{mass} = g_0 \frac{\left( \frac{m_{HEX}+m_{coolant}+}{m_{duct}+m_{pump}+m_{fan}} \right)}{L/D} \tag{11}$$

where $g_0 = 9.81\,\mathrm{m/s^2}$ and $L/D$ the lift-to-drag ratio of the aircraft at a given operating point. The component masses in Eq. (11) vary between cooling duct designs and the mass calculation procedure is given in Appendix A.4.

The drag force due to the air's loss of momentum inside the cooling duct is

$$D_{int} = -F_{net,\ uninst.} = \dot{m}_{air}(v_\infty - v_6) \tag{12}$$

and is simply the negative net uninstalled thrust from Eq. (6).

The power consumed by running the coolant pump is calculated by assuming a pump with an efficiency $\eta_{pump}$, see Table A.1. For the booster fan stage, the power consumed is the shaft power with a polytropic efficiency $\eta_{fan}$ and an electric efficiency $\eta_{fan,\ motor}$, again stated in Table A.1.

### 2.7.1. External drag

The external drag coefficient in Eq. (10) is estimated using the `ESDU 81024` method [27], which covers axisymmetric cowl geometries at various subsonic speeds and inlet mass flow conditions. The method calculates the total drag coefficient as

$$C_D = C_{D_p} + \Delta C_{D_s} + \Delta C_{D_w}$$

where $C_{D_p}$ is the profile drag coefficient and $\Delta C_{D_s}$ and $\Delta C_{D_w}$ the spillage and wave drag coefficient increments, respectively. The normalizing reference area is the cross-sectional area at the point of maximum diameter ($S_{ref} = A_{max}$). For the geometries and conditions covered in this paper, the freestream Mach number is below the drag-rise Mach number and therefore $\Delta C_{D_w}$ does not contribute. The spillage drag increment, however, will heavily penalize ducts operating below the critical mass flow ratio.

### 2.7.2. Duct geometry

The geometries covered in the ESDU drag method are NACA 1-series cowls [27]. In this study we split the cooling duct geometry into an internal and external geometry. The internal geometry consists of a spline lip geometry that transitions to a constant diffuser upstream of the heat exchanger, and a constant converging nozzle ramp profile in the back (as in Fig. 1). The outer and inner splines have an initial forebody radius set to match the NACA 1-series geometry used in [27]. The splines are generated using the class shape transformation (CST) method covered in [28]. The outer spline is constrained by a point of maximum diameter (see Fig. 2), which occurs at the streamwise position $x_{max} = x_3$ and has the radius $r_{max} = r_3 + (t_{max}/L_{tot})L_{tot}$, where $t_{max}/L_{tot} = 0.05$ is the thickness-to-length ratio and $L_{tot} = x_6 - x_0$ the total axial length of the duct.

The upper trailing edge tangent is offset 10° from the nozzle ramp angle. The location of the inlet throat is set as a function of the diffuser area ratio $AR_d$ and the diameter at the heat exchanger inlet face $d_3$. For $1.1 < AR_d < 2$, the lip contraction ratio varies according to

$$AR_l = 0.9 - \frac{(AR_d - 1.1)}{9}$$

and the streamwise location according to $x_1 = (L_{0\text{-}1}/d_3) \cdot d_3$, where

$$L_{0\text{-}1}/d_3 = 0.05 + \frac{(AR_d - 1.1)}{18}.$$

### 2.8. Modeling assumptions and limitations

The propulsive layout studied consists of two propellers, where each propeller is driven by its own motor, which is supplied with power from its own fuel cell system. The fuel cell is in turn cooled by its own ram-air cooling system. The complete ram-air cooling system model (Sections 2.5–2.7), represents one of the two cooling systems. The cooling requirement is defined for a single ram-air cooling system, which means that the presented designs and their resulting performance numbers (such as power draw, mass flow and weight) represent half of the values for the entire aircraft.

The cooling requirement for an operating point is fixed regardless of the resulting power draw as we are not updating the requirement through a drag-dependent sizing loop. This is done intentionally to maintain maximum comparability between designs, as the focus is on the ram-air cooling physics. A limitation of this modeling assumption is that designs with very poor performance, e.g. a cooling system drawing power on the order of the heat rejection requirement, might not only be infeasible due to the inability of the fuel cell system to provide that amount of power, but also because the actual heat rejection requirement might be even higher due to snowball effects. With this in mind, it is expected that the relevant portion of the design space surrounding the optima will consume around 10 % to 20 % of the fuel cell system's gross power output, making this assumption acceptable.

For the internal drag calculation in Eq. (12), it can be seen that for $v_6 > v_\infty$, the cooling system is free of internal drag and instead produces thrust. If the thrust generation is large enough to turn the total drag $D_{total}$ in Eq. (9) negative, then this will cause $P_{drag}$ in Eq. (8) to also go negative. In this particular case, we assume that the aircraft's required thrust generation is partially covered by the cooling system. The details on the aircraft control system itself and how thrust is controlled are beyond the scope of this paper. Nevertheless, if the total power draw $P_{total}$ remains positive (which is expected), the fuel cell system must still provide power to the cooling system.

Regarding the correlation method used for estimating the external drag (Section 2.7.1), some allowances are made to facilitate the design space exploration. For the case of a cooling duct design operating at MFR > 1 (e.g. a small inlet at take-off with a large fan pressure ratio), the method is undefined. In order to get an external drag estimate for situations where MFR > 1, we calculate the drag as if MFR = 1. We allow for this approximation when $M_\infty < 0.2$, as the performance penalty in this scenario will be dominated by the internal losses and the power used by the fan. Designs exhibiting MFR > 1 at $M_\infty > 0.2$ are considered infeasible and are discarded from the study.

The correlation method for calculating the inlet total pressure loss (Appendix A.2.1) is used throughout this study, despite the discrepancies in drag it causes at higher nozzle area-ratios (see Appendix B). At the relevant low nozzle area-ratios, the difference is minimal. Using the inlet loss model in this way represents a conservative performance assumption in terms of drag estimation. To maintain this conservative approach and thereby ensuring that our results are robust to parameter uncertainty, we have kept this model enabled throughout the usage of the quasi-1D code. The observed discrepancy in mass flow between the quasi-1D and CFD solutions (Appendix B) are clearly stated in the paper, but we have not updated the quasi-1D code to correct for these changes.

**Table 2**
Design variables for optimization. Variables marked by (*) are state variables that are treated as design variables depending on operating condition (see Section 2.5).

| Parameter | Bounds |
|---|---|
| *Heat-exchanger* | |
| $L_x$ | (0.05–1) m |
| $\sigma_r$ | (0.02–50) |
| $\alpha_r$ | (0.05–20) |
| $\chi$ | (0.01–1) |
| $\Delta T_{\text{coolant}}$ * | (1–15) K |
| *Cooling duct* | |
| $A_0$ | (0.1–4) m$^2$ |
| $\text{AR}_d$ | (1–2) |
| $\theta_d$ | (4–10)° |
| $\pi_{\text{fan}}$ * | (1–1.1) |
| $\text{AR}_n$ * | (0.01–1) |

## 3. Design optimization

Using the introduced methodology, we are able to evaluate the performance of a particular cooling design concept, in a chosen set of operating points. By design concept, we mean a combination of free design variables that together with the fixed parameters in Table A.1 fully define the combined system of cooling duct and heat exchanger. The free design variables and their optimization bounds are listed in Table 2. By giving numeric values to both the free design variables and the fixed parameters a cooling design becomes fully defined.

The best combination of design variables will be the one that minimizes the parasitic power draw described in Section 2.7. The magnitude of the parasitic power draw can differ greatly between two operating points. To establish the best conceptual design, we define the optimization cost function to be a weighted sum of the set of operating points

$$P_{\text{total}} = \sum_i b_i P_i \,, \tag{13}$$

where $P_i$ is the total power draw in an operating point and $b_i$ its bias factor ($\sum_i b_i = 1$). The bias factors are set up to reflect the mission that the aircraft is designed for.

### 3.1. Numerical optimization

To perform the optimization study, we use the package `optiMagic` [29] to run a global multistart optimization with `Subplex` [30,31] as the local optimization method. The best global result is then used as a starting point for a final local optimization with Subplex, to polish the solution and get closer to the optimum. In optiMagic the multistart exploration phase is done with a Sobol sampling and the number of samples is set to $1000n$, where $n$ is the number of design variables. The best 100 points in the exploration phase are then used in the multistart method. The multistart strategy results in a broad exploration of the design space and lessens the chance of getting stuck in a local minima.

## 4. Results

The operating points considered in the design optimization study are a hot-day take-off (”Hot T-O”) and a cruise (”Cruise”). The hot day take-off is the most critical point for the cooling system to provide enough heat removal for the fuel cell to continue to work. At the same time, the cruise point needs to be included since this point governs the overall efficiency of the solution. Hence, using the bias factors of Eq. (13) allows us to minimize the energy used during cruise, while also making sure that the most difficult and constraining operating point, the hot take-off, is cleared at a feasible power usage.

**Table 3**
Operating points used to evaluate the designs.

| | Hot T-O | Cruise |
|---|---|---|
| $M_\infty$ | 0.17 | 0.45 |
| $h$ | 0 m | 6400 m |
| $\Delta T_{\text{ISA}}$ | 25 K | 0 K |
| $Q_{\text{req.}}$ | 2 MW | 1.2 MW |
| $L/D$ | 10 | 17 |
| $b$ | 0.2 | 0.8 |

**Table 4**
Resulting cruise-only geometries.

| | | Front fan | Rear fan |
|---|---|---|---|
| *Heat exchanger* | | | |
| $A_{fr_{\text{air}}}$ | m$^2$ | 1.517 | 1.517 |
| $L_x$ | m | 0.350 | 0.372 |
| $\sigma_r$ | – | 21.121 | 23.405 |
| $\alpha_r$ | – | 6.729 | 7.373 |
| $\chi$ | – | 0.0476 | 0.0426 |
| *Cooling duct* | | | |
| $A_0$ | m$^2$ | 1.153 | 1.150 |
| $A_{\text{max}}$ | m$^2$ | 2.229 | 2.235 |
| $d_0$ | m | 1.212 | 1.210 |
| $d_3$ | m | 1.390 | 1.390 |
| $d_{\text{max}}$ | m | 1.685 | 1.687 |
| $L_{\text{tot}}$ | m | 2.947 | 2.973 |
| $\text{AR}_d$ | – | 1.548 | 1.552 |
| $\theta_d$ | ° | 10 | 10 |

The flight conditions are set assuming a regional fully electric fuel cell aircraft comparable to an ATR 72 in terms of flight performance. The cooling requirement is set to 2 MW for take-off and 1.2 MW for cruise, which is in line with studies [17,32] of similar sized fuel cell aircraft. The operating points and the remaining parameters are described in Table 3.

The rationale and approach of the study is to understand how the operating conditions relate to the power draw of the cooling system. More specifically, interest is taken in how the constraint imposed by the hot-day take-off operating point influences the design parameters. To achieve this, we first compute an optimal configuration purely designed for the cruise operating point, labeled *“Cruise-only”*. Next, another type of optimal configuration is computed, which is able to clear the hot-day take-off operating point in addition to the cruise. We call this take-off-capable configuration the *“Dual-point”* design. The cruise-only configuration establishes a benchmark “best-case scenario” design which the dual-point design may be compared to. By doing this, we are able to quantify the performance penalty of having a take-off compatible design. For both the cruise-only and dual-point configurations, we investigate two fan layouts: a fan mounted upstream of the heat exchanger between station 2 and station 3 (*“Front fan”*) and a fan mounted downstream between station 4 and station 5 (*“Rear fan”*).

### 4.1. Cruise-only optimal designs

For a cruise-only design with a reasonably sized duct and heat exchanger, the mass flow generated by the ram-pressure alone is enough to satisfy the cooling need. Operating a booster fan is therefore not a necessity. A possible optimum configuration could then be a system with a fan total pressure ratio $\pi_{\text{fan}} = 1$, i.e. zero fan shaft power, which in turn reduces mass and total power draw. Regardless, the fan total pressure ratio is still available as a design variable to the optimizer. The resulting optimal geometries for the two designs are found in Table 4. The system-level and aerothermal performance of the two designs are presented in Table 5.

**Table 5**
Performance breakdown of the cruise-only designs.

| | | Front fan | Rear fan |
|---|---|---|---|
| *Power* | | | |
| $P_{drag}$ | kW | −17.697 | 53.728 |
| $P_{pump}$ | kW | 2.877 | 3.351 |
| $P_{fan}$ | kW | 66.642 | 0.000 |
| $P_{total}$ | kW | 51.821 | 57.080 |
| *Drag* | | | |
| $D_{mass}$ | N | 118.9 | 98.4 |
| $D_{int}$ | N | −523.8 | −123.1 |
| $D_{ext}$ | N | 310.0 | 313.0 |
| $D_{total}$ | N | −94.9 | 288.3 |
| *Mass* | | | |
| $m_{duct}$ | kg | 73.7 | 74.7 |
| $m_{HEX}$ | kg | 69.0 | 65.7 |
| $m_{coolant}$ | kg | 23.5 | 22.8 |
| $m_{pump}$ | kg | 6.4 | 7.4 |
| $m_{fan}$ | kg | 33.3 | 0.0 |
| $m_{total}$ | kg | 206.0 | 170.5 |
| *Aerothermal performance* | | | |
| $\dot{m}_{air}$ | kg/s | 18.0 | 17.4 |
| $\dot{m}_{coolant}$ | kg/s | 38.3 | 41.1 |
| $\pi_{tot}$ | – | 1.020 | 0.982 |
| $\pi_d$ | – | 1.000 | 1.000 |
| $\eta_d$ | – | 0.996 | 0.996 |
| $\pi_{HEX,\ air}$ | – | 0.982 | 0.982 |
| $\pi_{HEX,\ coolant}$ | – | 0.884 | 0.875 |
| $\pi_{fan}$ | – | 1.040 | 1.000 |
| $\epsilon$ | – | 0.716 | 0.712 |
| $T_{03}$ | K | 260.2 | 256.6 |
| $\Delta T_{coolant}$ | K | 8.6 | 8.1 |
| MFR | – | 0.174 | 0.169 |
| NPR | – | 1.173 | 1.128 |
| $AR_n$ | – | 0.139 | 0.155 |
| $F_{gross}$ | N | 3067.8 | 2583.0 |

#### 4.1.1. Front fan cruise-only design

First, the cruise-only optimized design with an upstream-mounted fan is presented ("Front fan" in Fig. 3, Tables 4, 5). The optimal inlet is predicted to have an inlet area of 1.15 m$^2$ and a diffuser area ratio of 1.55. The duct's maximum diameter is 1.69 m and the total length 2.95 m.

The air-streamwise length $L_x$ of the heat exchanger is short, about a fourth of the local duct diameter $d_3$. The void fraction ratio $\sigma_r$ is relatively high which is due to the air side being much more limiting than the coolant side, and hence requires more volume. The limiting nature of the air side is further confirmed by the surface area density ratio $\alpha_r$, which shows the air side having a roughly seven times larger surface area than the coolant side. The solidity factor $\chi$ is relatively low, indicating a low compactness of the heat exchanger. A more compact heat exchanger could have been achieved if either the diameter or the air-streamwise length were made smaller, at the expense of increasing the total pressure loss in both the air and coolant streams.

The overall total pressure ratio $\pi_{tot}$ in the cooling duct is above one, as the optimization found benefit in using the front-mounted fan. The resulting fan total pressure ratio was $\pi_{fan} = 1.04$. As for the loss of total pressure experienced across the inlet, diffuser and heat exchanger, it is rather low at 1.9 % (Table 5). Most of the loss occurs in the heat exchanger, as the diffuser total pressure ratio is practically equal to one (for three decimal places). We therefore also include the diffuser adiabatic efficiency $\eta_d$ in Table 5. The diffuser performance is explained by the low MFR, which has the effect of shifting the captured streamtube's stagnation point further downstream (inside the duct), preventing any form of internal lip separation. The low MFR is caused by the oversizing of the duct inlet, which has the favorable effect of pressurizing the air externally, upstream of the duct. The oversizing is balanced against the spillage drag, which occurs below a critical mass flow ratio that is dependent on diffuser area ratio. By increasing the area ratio, the slope

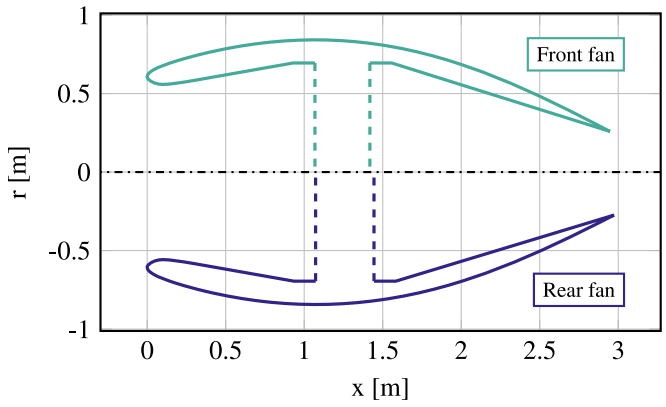



**Fig. 3.** Cross-sections of the cruise-only optimized front fan variant (top) and the rear fan variant (bottom).

of the initial forebody aligns better with the streamlines, lowering the critical mass flow ratio.

From the performance breakdown of the front fan case (Table 5), we see that the total drag $D_{total}$ and its associated drag power $P_{drag}$ consist of three large terms. The drag related to the momentum of the internal flow $D_{int}$ is negative, meaning that a net (uninstalled) thrust is being generated instead of drag. This increase in internal momentum manages to fully cancel out the drag caused by the added mass $D_{mass}$ and the external nacelle drag $D_{ext}$, and is enough to turn the total drag $D_{total}$ negative (net installed thrust). This increase in momentum is established primarily by the increased pressure due to the fan but also due to the Meredith effect [5] caused by the heat transfer and subsequent temperature increase. The total power draw of the cooling system $P_{total}$ is still positive, due to the power required to run the fan $P_{fan}$ and a smaller contribution associated with the circulation pump $P_{pump}$. The total system weight is 206.0 kg and is dominated by the heat exchanger and duct mass. In total, the system consumes 51.8 kW during cruise operation (Table 5).

Whether it is beneficial at all to include a fan is actually determined by the polytropic efficiency of the fan. If the fan efficiency is lowered, the temperature of the air entering the heat exchanger increases. This reduces the temperature difference between the coolant and the air inside the heat exchanger, which in turn reduces the heat rejection. This leads to a need to increase the heat exchanger surface area, resulting in increased mass. The surface area of the heat exchanger can be made larger by increasing the diameter or by making it denser, both of which increase the drag. On the positive side, the upstream fan helps to reduce the air-side pressure loss across the heat exchanger by reducing the flow speed, and a large part of the power used for this pressure increase is returned by increasing the momentum of the fluid and generating thrust. When reducing the fan efficiency from 80 % to 70 %, the optimizer predicted a 1.0 total pressure ratio as optimal, which implies that no fan should be used. As we will see for the rear fan case, the optimizer predicts that no fan should be used even for the nominal efficiency of 80 %. For the dual-point cases, that is when take-off is included, a fan is always beneficial since it is needed to meet the much higher take-off heat transfer requirement.

#### 4.1.2. Rear fan cruise-only design

We now turn our attention to the cruise-only optimal design with the fan mounted downstream of the heat exchanger ("Rear fan" in Fig. 3, Tables 4, 5). The resulting duct also has an inlet area of 1.15 m$^2$ and a diffuser area ratio of 1.55, and is marginally smaller than the front fan variant. This results in a maximum diameter of 1.69 m of the duct, and a total length of 2.97 m.

The heat exchanger has a slightly larger air-streamwise length compared to the front fan variant's. Comparing the heat exchanger

parameters, the void fraction ratio and surface area density ratio have increased slightly while the solidity has decreased. Although the heat exchanger and duct geometries differ slightly from the front fan variant, the air-side total pressure loss remains practically the same. On the coolant side, the total pressure loss has increased slightly.

The optimization did not find any benefit to using a rear fan, which is manifested by the fact that the optimizer predicts a fan total pressure ratio of 1.0 ($\pi_{\text{fan}} = 1$). Thus, the main difference from the front fan configuration is that the cooling system has traded away a large part of the increase in internal momentum for a zero fan power requirement ($P_{\text{fan}} = 0.0\,\text{kW}$). The pump power is slightly higher when compared to the front fan case, which is expected as the coolant mass flow and pressure loss are increased. The overall weight of the system is 17.2 % lower than the front fan variant. This is mainly due to the removal of the fan, which removed 33.3 kg compared to the front fan installation. In total, this configuration requires 10.1 % more power compared to the front fan variant.

When comparing the front fan and rear fan variants, it can be seen that the main benefit from the upstream fan placement is that it contributes to reducing the pressure loss over the heat exchanger (which would otherwise be higher), but as noted in the analysis for the front fan variant, the overall benefit is easily canceled from a reduced fan efficiency where the reduction in heat transfer due to increased heating of the inlet air starts to dominate.

#### 4.1.3. Cruise-only designs evaluated at take-off

If the cruise-only rear fan design is run in the take-off operating point, the infeasibility of this design to fulfill a mission becomes obvious. The rear fan configuration is able to achieve 0.421 MW of cooling (at the same $\text{AR}_n$ and $\pi_{\text{fan}}$ as in Table 5), which is far from the required 2 MW. The front fan configuration is somewhat better in take-off, but still far from the target, delivering a 0.550 MW of cooling with the same fan total pressure ratio and nozzle area ratio as in Table 5.

It was then investigated how close the two variants could get to the cooling target of 2 MW, by varying the previously fixed nozzle area ratio, fan total pressure ratio and coolant temperature drop. For the front fan variant, the resulting optimal parameters $\text{AR}_n = 0.925$, $\pi_{\text{fan}} = 1.0737$ and $\Delta T_{\text{coolant}} = 3.8\,\text{K}$ resulted in a maximum cooling of 1.283 MW. However, this raised the fan power to 767.3 kW and the pump power to 87.9 kW. The air mass flow of 92.3 kg/s caused a maximum Mach number of 0.24 inside the duct, which occurred in the throat. It is then clear that the front fan variant has a ceiling for the maximum achievable cooling which is set by the best compromise of rise in temperature and the inlet total pressure loss, as mass flow can be increased with increased fan total pressure ratio, at the cost of the temperature increasing. For the rear fan variant, the 2 MW cooling target was achieved with $\text{AR}_n = 1.0$, $\pi_{\text{fan}} = 1.261$ and $\Delta T_{\text{coolant}} = 3.6\,\text{K}$. However, this required an unrealistic 4.371 MW of fan power and 95.721 kW for the coolant pump. The resulting mass flow was 150.7 kg/s and no choking was observed. At this state, the cooling duct was able to produce 5.8 kN of uninstalled net thrust. The ceiling for the rear fan variant's maximum cooling, which was not yet reached here, is set by the loss of total pressure in the duct, as the rear fan does not raise the heat exchanger inlet temperature. When the ceiling is reached, the heat rejection cannot be increased further, as increasing the fan total pressure ratio does not increase the mass flow rate fast enough to compensate for the decreasing heat exchanger effectiveness.

### 4.2. Dual-point optimal designs

As the name suggests, the dual-point optimal design must meet the cooling need in both the operating points described in Table 3. In take-off the ram-pressure is insufficient and the fan is needed to increase the total pressure and thereby the mass flow of air. Here, the optimizer also has the option of changing to a different nozzle area ratio and coolant temperature drop than what is used in the cruise operating point. The mass of the fan and the coolant pump are set by their individual highest power consumption, i.e. the take-off could be dimensioning for the pump and cruise for the fan. Lastly, we again consider a front fan variant and a rear fan variant.

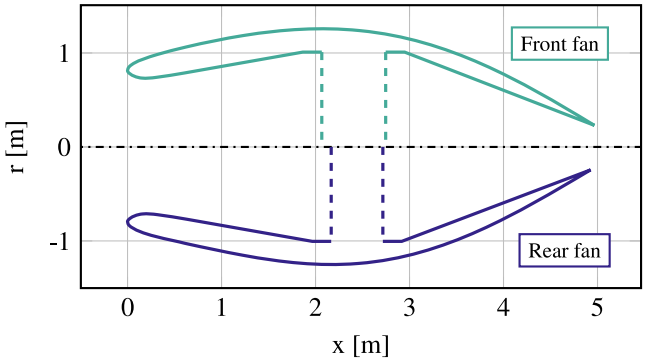



**Fig. 4.** Cross-sections of the dual-point optimized front fan variant (top) and the rear fan variant (bottom).

**Table 6**
Resulting dual-point geometries.

| | | Front fan | Rear fan |
|---|---|---|---|
| *Heat exchanger* | | | |
| $A_{fr_{\text{air}}}$ | $\text{m}^2$ | 3.200 | 3.171 |
| $L_x$ | m | 0.680 | 0.550 |
| $\sigma_r$ | – | 25.355 | 22.454 |
| $\alpha_r$ | – | 6.414 | 6.865 |
| $\chi$ | – | 0.0351 | 0.0417 |
| *Cooling duct* | | | |
| $A_0$ | $\text{m}^2$ | 2.072 | 1.985 |
| $A_{\text{max}}$ | $\text{m}^2$ | 4.969 | 4.917 |
| $d_0$ | m | 1.624 | 1.590 |
| $d_3$ | m | 2.019 | 2.009 |
| $d_{\text{max}}$ | m | 2.515 | 2.502 |
| $L_{\text{tot}}$ | m | 4.967 | 4.927 |
| $\text{AR}_d$ | – | 1.906 | 1.996 |
| $\theta_d$ | ° | 10 | 10 |

#### 4.2.1. Front fan dual-point design

We first examine the dual-point optimal design with a front fan ("Front fan" in Fig. 4, Tables 6, 7). Compared to the front fan cruise-only design, the inlet area has grown by 79.7 % and its maximum diameter by 49.3 %. This brings the maximum diameter to 2.52 m. The overall length of the system is 4.97 m, which is an 68.5 % increase over the cruise-only counterpart. The heat exchanger has increased in both in the air-streamwise length and diameter, and its length-to-diameter ratio is about a third. Both the heat exchanger surface area density ratio and solidity have decreased, while the void fraction is similar. The weight of the system has increased almost threefold over its cruise-only counterpart. The fan is used in both take-off and cruise, with the fan total pressure ratio reaching 1.05 in cruise. The total weighted power draw was 169.2 kW.

In take-off 304.7 kW of power is consumed. This corresponds to 15.2 % of the total stack power given a fuel cell efficiency of 50 %. About a third of the total power requirement, 109.8 kW, is consumed by the fan. The pump power has risen considerably and is no longer insignificant at 21.9 kW, which is on the one hand due to the higher required cooling in the take-off point, but also because the decrease in coolant temperature drop, which increases the coolant mass flow and thereby convection, is traded against an increased total pressure loss. As for the drag force, the low freestream velocity causes the drag to be dominated by the internal drag (63 % of total) and weight drag (26 %). The external drag only makes up 11 % of the total.

**Table 7**
Performance breakdown of the dual-point designs.

| | | Front fan | | Rear fan | |
|---|---|---|---|---|---|
| | | T-O | Cruise | T-O | Cruise |
| *Power* | | | | | |
| $P_{drag}$ | kW | 172.9 | 55.2 | 125.6 | 140.2 |
| $P_{pump}$ | kW | 21.9 | 0.334 | 20.3 | 0.409 |
| $P_{fan}$ | kW | 109.8 | 79.8 | 146.8 | 0.0 |
| **Total** | kW | 304.7 | 135.3 | 292.8 | 140.6 |
| *Drag* | | | | | |
| $D_{mass}$ | N | 569.5 | 335.0 | 564.4 | 332.0 |
| $D_{int}$ | N | 1380.9 | −724.6 | 792.6 | −256.4 |
| $D_{ext}$ | N | 228.7 | 685.8 | 226.1 | 676.6 |
| **Total** | N | 2179.2 | 296.2 | 1583.1 | 752.2 |
| *Mass* | | | | | |
| $m_{duct}$ | kg | 186.5 | | 185.0 | |
| $m_{HEX}$ | kg | 208.4 | | 198.5 | |
| $m_{coolant}$ | kg | 82.0 | | 73.3 | |
| $m_{pump}$ | kg | 48.8 | | 45.2 | |
| $m_{fan}$ | kg | 54.9 | | 73.4 | |
| **Total** | kg | 580.6 | | 575.3 | |
| *Aerothermal performance* | | | | | |
| $\dot{m}_{air}$ | kg/s | 77.6 | 15.1 | 74.4 | 14.1 |
| $\dot{m}_{coolant}$ | kg/s | 131.1 | 25.4 | 118.3 | 25.6 |
| $\pi_{tot}$ | – | 0.989 | 1.051 | 0.992 | 0.994 |
| $\pi_d$ | – | 0.999 | 1.000 | 0.999 | 1.000 |
| $\eta_d$ | – | 0.933 | 0.998 | 0.928 | 0.998 |
| $\pi_{HEX,\ air}$ | – | 0.978 | 0.994 | 0.978 | 0.994 |
| $\pi_{HEX,\ coolant}$ | – | 0.744 | 0.980 | 0.737 | 0.975 |
| $\pi_{fan}$ | – | 1.012 | 1.057 | 1.016 | 1.000 |
| $\epsilon$ | – | 0.697 | 0.862 | 0.701 | 0.874 |
| $T_{03}$ | K | 316.3 | 261.7 | 315.0 | 256.6 |
| $\Delta T_{coolant}$ | K | 4.2 | 13.0 | 4.7 | 12.9 |
| MFR | – | 0.551 | 0.082 | 0.551 | 0.080 |
| NPR | – | 1.009 | 1.208 | 1.013 | 1.142 |
| $AR_n$ | – | 0.551 | 0.052 | 0.458 | 0.059 |
| $F_{gross}$ | N | 3301.4 | 2870.6 | 3694.1 | 2260.6 |

During take-off, the heat exchanger achieves a similar effectiveness as the cruise-only design did in cruise, but requires a fourfold increase in air mass flow. A twofold increase can be attributed to the roughly double cooling requirement, with the other half explained by the now much degraded temperature difference between the fuel cell stack and the ambient. In take-off, the temperature difference between the air and coolant inlet is only 38 K, compared to the cruise point's 97 K. To provide the mass flow, the front-mounted fan has to increase the total pressure by 1.2 %. The air loses 1.1 % of its total pressure across the duct, with 2.2 % of the loss occurring in the heat exchanger (compared to the cruise-only's 1.8 %) and 0.1 % in the inlet-diffuser section. Regarding the coolant, the optimizer found it beneficial to have a relatively low coolant temperature drop, as this increases the mass flow. The loss of total pressure inside the coolant is high at 25.6 %, which explains the large power draw of the pump during take-off. An inlet mass flow ratio (MFR) of 0.55 is observed, and the nozzle area ratio results in an exit area of 1.96 $m^2$, which is 85 % of the inlet area.

In cruise the overall power consumption was 135.3 kW. This is a 161 % increase compared to the cruise-only front fan counterpart. Just as in the cruise-only case, the front fan is used to great effect with a large drag reduction observed, but was overall not able to produce a net installed thrust. Almost 71 % of the drag is canceled by the thrust, and the fan required 79.8 kW to do so. During cruise, 15.1 kg/s of air is needed to satisfy the cooling requirement. This is a 16 % decrease compared to the cruise-only result.

The overall total pressure ratio across the system during cruise is like in the cruise-only case, above one, with the fan increasing the total pressure by 5.7 % and the overall loss across the inlet and heat exchanger amounting to 0.6 %. Compared to the cruise-only result, the overall total pressure loss is decreased by 1.2 %. For the coolant mass flow, a 33.7 % reduction is observed, which is due to the one and a half times larger coolant temperature drop. The coolant side experiences a relatively low loss of total pressure, at only 2.0 % compared to the cruise-only's 11.6 %. The MFR is observed to be very low at 0.082 and the cruise nozzle exit area is 0.166 $m^2$.

#### 4.2.2. Rear fan dual-point design

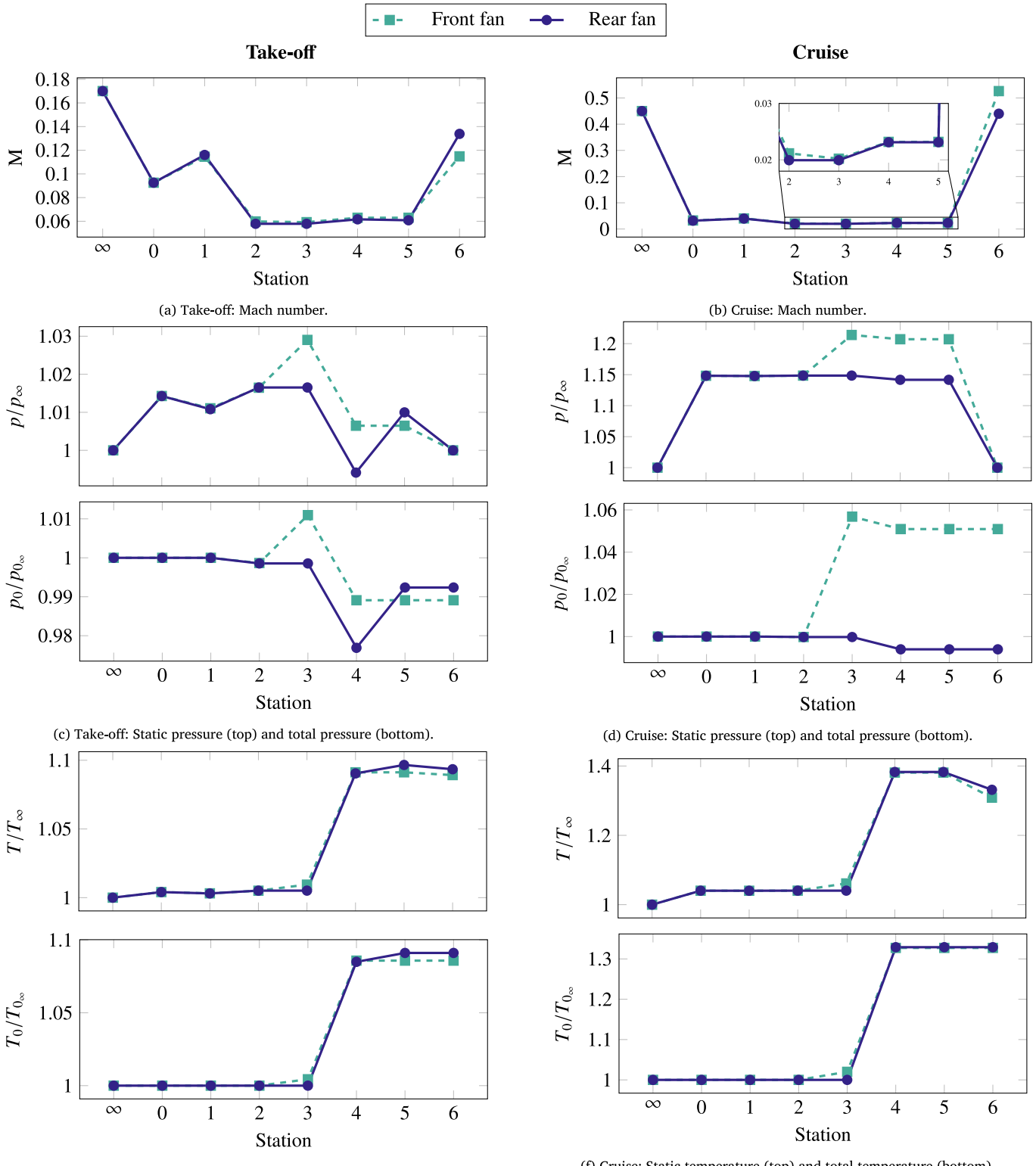
The rear fan variant of the dual point optimal design is now presented ("Rear fan" in Fig. 4, Tables 6, 7). The inlet area has increased by 72.6 % compared to its cruise-only counterpart, and together with a diffuser area ratio of almost 2, the resulting maximum diameter of the duct is 2.50 m, which is a 48.3 % increase. The overall length has increased by 65.7 % and now measures 4.927 m. Compared to the cruise-only counterpart, the heat exchanger has more or less the same solidity, but with a slightly smaller void fraction ratio and surface area density ratio. As a result, the heat exchanger is denser when compared to the front fan dual-point design, and therefore has a shorter air-streamwise length. The total weight of the system is 575.3 kg, which is similar to the front fan version. The rear-mounted fan is used for take-off, but was like in the cruise-only case not used for cruise, even though this would not bring any further weight penalty. The overall weighted power draw was 171.0 kW, which makes it 1.1 % worse than the front fan dual-point design.

In take-off the total power draw was 292.8 kW, with the fan consuming the most followed by the drag and the coolant pump. Compared to the dual-point front fan design, the fan power consumption increased by 33.7 %, while the pump power remained similar. The aerothermal performance is also similar, but with a slight decrease in both air and coolant mass flow, as the rear fan variant does not suffer from elevated heat exchanger inlet temperatures on the air side as in the case of the front fan. The overall total pressure loss for the air side is practically the same as in the front fan case. On the coolant side, the total pressure loss is increased, but is on the other hand having a lower mass flow, which explains the marginally lower pumping power. The drag force is similar to that of the front fan dual-point variant with the exception of the internal drag, which is almost halved.

In cruise the overall power consumption was higher compared to the dual-point front fan variant, at 140.6 kW which is a 3.9 % increase. Shifting the comparison to the rear fan cruise-only variant, this is a 146 % increase. The power draw is practically only due to drag, as the fan was not used and because the pump only needed 0.41 kW (compared to the cruise-only's 3.35 kW). The drag is again dominated by the external drag, followed by the weight induced drag. The system is able to produce thrust again and was therefore able to offset 25 % of the weight and external drag. The duct operated at an MFR of 0.080 and the nozzle exit area was 0.187 $m^2$.

### 4.3. Further dual-point analysis

In take-off, the dual-point front fan variant consumes 4.1 % more power compared to the rear fan variant. In cruise the situation is reversed, where the front fan variant instead consumes 3.8 % less power. Overall, it can be said that the two variants perform very similarly based on the weighted power draw, but achieve their performance very differently. As in the cruise-only results, the front fan variant uses the fan during cruise to increase the total pressure, which lessens the heat exchanger losses and increases the thrust. The increase in heat exchanger inlet temperature during cruise was not large enough to nullify the power saved by the extra thrust generation. It is rather in take-off where the negative aspects of the front fan become more apparent. To compensate for the slight increase in inlet temperature, both the air and coolant mass flows had to increase. The size of the heat exchanger then has to grow in order to maintain the level of total pressure loss. All of this leads to a slightly heavier and larger system, which increases the external drag during cruise. Regardless, the front fan is more efficient at




(a) Take-off: Mach number.

(b) Cruise: Mach number.

(c) Take-off: Static pressure (top) and total pressure (bottom).

(d) Cruise: Static pressure (top) and total pressure (bottom).

(e) Take-off: Static temperature (top) and total temperature (bottom).

(f) Cruise: Static temperature (top) and total temperature (bottom).

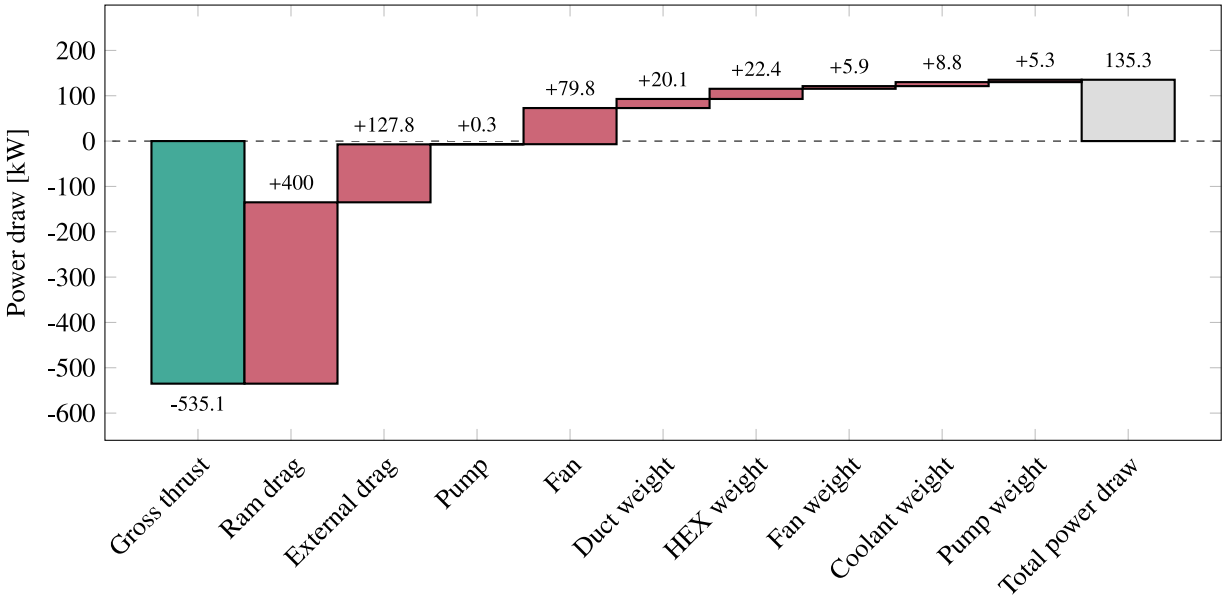
**Fig. 5.** Variation of pressure, temperature and Mach number throughout the cooling duct in the dual-point designs. Normalized by freestream station value.

increasing the pressure of the fluid, and therefore the power draw is less than in the rear fan variant.

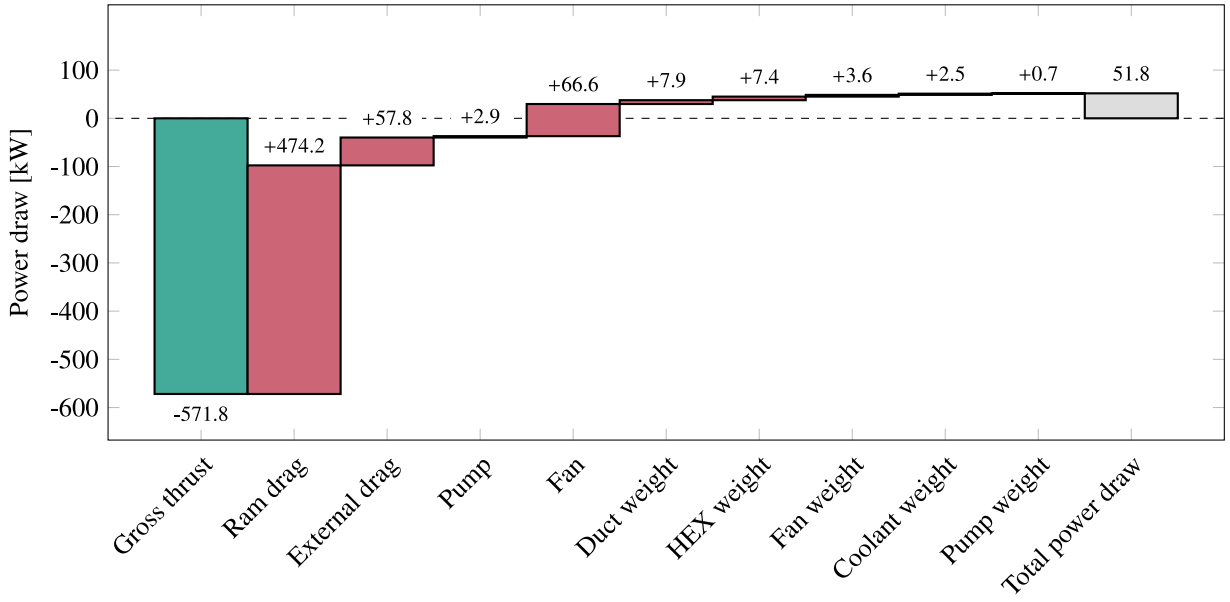
In cruise, the mass flow ratio for both variants has decreased when compared to their cruise-only counterparts. Furthermore, the dual-point designs have larger diffuser area ratios, and are therefore diffusing the flow more than in the cruise-only designs. As is seen in Fig. 5d, the front fan dual-point design manages to increase the static pressure by around 15 % (similar performance was observed in the cruise-only designs) between the freestream and the diffuser exit, with the external streamtube diffusion performing a majority of the pressurization. At the intake face (station 0) of the front fan dual-point design, the ratio of static pressure to total pressure is $p_0/p_{0_\infty} = 99.4\,\%$, i.e. almost all of the

freestream dynamic pressure has been converted into static pressure. The Mach number has then been reduced from 0.45 in the freestream to 0.033 at the intake face (Fig. 5b). The diffuser and fan then further diffuses the cooling air, until it reaches a Mach number of 0.020 just upstream of the heat exchanger. The near full recovery of the dynamic pressure, and the fact that it mostly occurs upstream of the intake, indicates that the optimization has maximized the use of intake oversizing, as further increasing the inlet size would not yield any meaningful increase in static pressure. Upon further investigation, it was found that the optimal designs consistently had mass flow ratios (MFR) virtually equal to the critical mass flow ratio for the onset of spillage drag. The dual-front designs were therefore on the limit of, but not yet suffering from spillage drag.

The two heat exchangers have quite low solidity and are in general terms not very compact. This is a result of the previously mentioned tendency to maximize the external streamtube diffusion, which results in large internal duct diameters. In other words, the optimizations have found more benefit in having large designs with low loss of total pressure, but larger external drag, instead of more compact designs with less external drag. The extra external drag is then worth it, as the large size allows the design to utilize the full amount of available ram pressure and to have very low airspeeds inside the heat exchanger and thereby a low amount of pressure loss, both of which are important for thrust generation. The heat exchanger is then able to reach the required cooling targets with a relatively open core, which explains the lack of compactness.

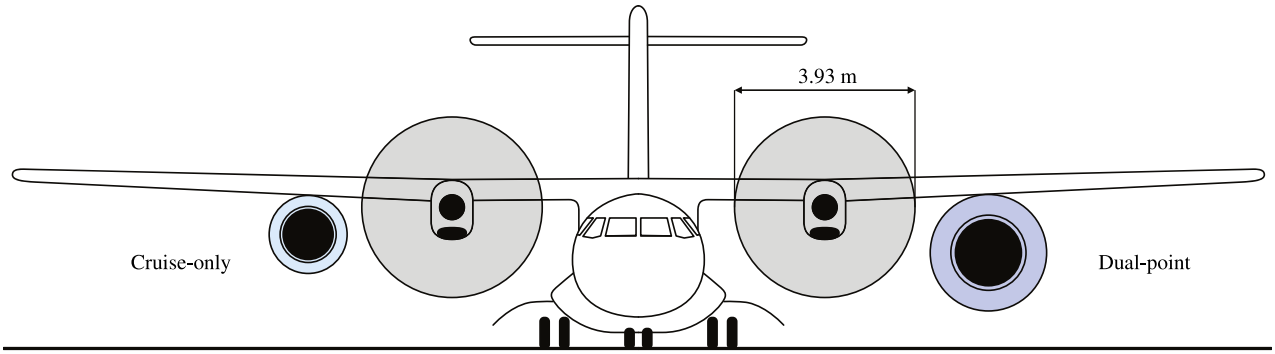



(a) Dual-point front fan in cruise.

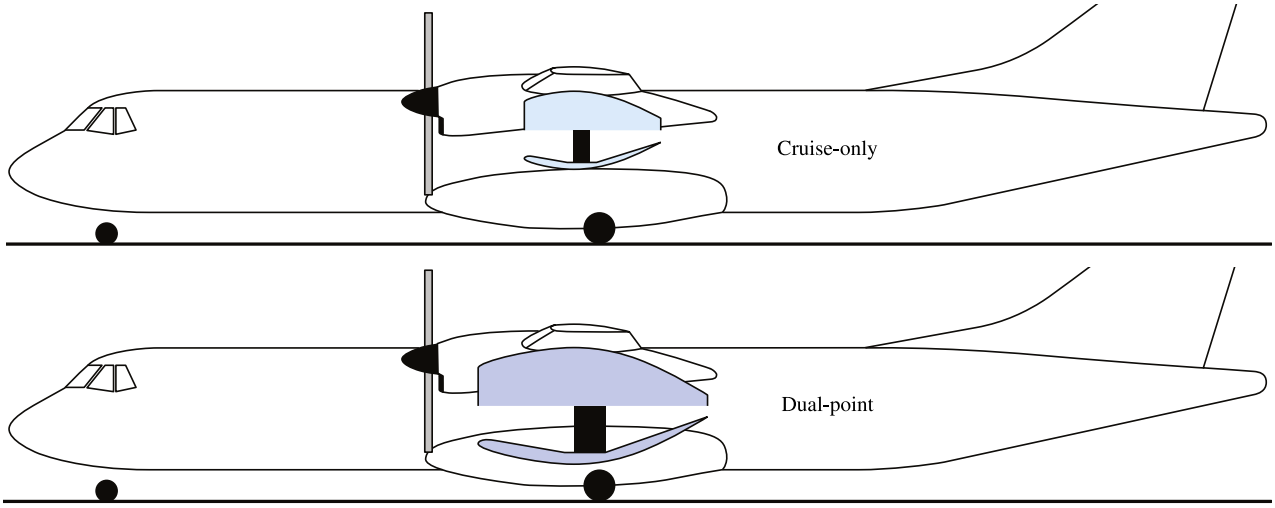



(b) Cruise-only front fan in cruise.

**Fig. 6.** Power draw in cruise for the dual-point and cruise-only designs. Both plots show the front fan configuration. A green bar represents a power saving, while a red bar represents power consumption. The total power draw is shown by the grey bar to the right. (For interpretation of the references to color in this figure legend, the reader is referred to the web version of this article.)




(a) Front view.




(b) Side view.

**Fig. 7.** Conceptual illustration of the cruise-only and dual-point front fan designs in relation to an ATR 72. For size comparison reasons only, no detailed integration considered.

In terms of feasibility the two designs clear the take-off point and do so within feasible overall power draws, as the total power consumption of the cooling duct would be around 15 % of the assumed total fuel cell stack power. We furthermore consider the fan and pump power consumptions to be within reasonable limits in take-off, even with the conservative efficiency assumptions. In cruise, the two designs consume around 11 % of the assumed stack power. In terms of the maximum diameter and overall length, the two designs are quite large and would be difficult to integrate in an existing airframe. With the axisymmetric layout covered in this study, the cooling duct could be mounted under the wing like the turbofan nacelle is in a conventional jet aircraft. A visual comparison of the cooling duct sizes is done in Fig. 7, where the cruise-only and dual-point designs are compared to an ATR 72 with its conventional propeller and turboprop powerplant. A different layout of the ducted heat exchanger could prove beneficial in terms of footprint and reduce external drag, such as considering heavily inclined heat exchangers inside non-axisymmetric ducts or scoop duct integrated into the fuselage. However, these designs would most likely complicate the fan integration and could severely increase the internal pressure losses. Regardless, all of this is dependent on how much and when the cooling is needed.

### 4.4. Power draw analysis

The manner in which each category of power draw contributes to the total consumption is visualized in Fig. 6 for the front fan variants of the dual-point and cruise-only designs. It is clearly seen that the effect of net thrust (gross thrust minus ram drag) is a dominant factor. This is an expected outcome of the optimization, as it is the only means of creating a negative contribution (a power saving) to the overall power draw. All other categories in the power draw are positive increments, and their impact can only be limited by minimizing their magnitude.

Both the dual-point and cruise-only designs benefit greatly from the net thrust. The dual-point (Fig. 6a) is able to fully rectify the external drag contribution, and does so with a 5.7 % margin. The cruise-only design (Fig. 6b) does the same, but with a 68.9 % margin. The dual-point design is able to produce a larger uninstalled net thrust than the cruise-only design, and does so by having a significantly lower ram drag, which can be attributed to the lower mass flow of air. This makes the larger design advantageous in terms of internal drag, but is not enough to offset the increase in external drag due to its increased cross sectional profile.

The next large category of power draw is the shaft power used to drive the front-mounted fan. Here, the dual-point and cruise-only designs are performing quite similar, with the dual-point consuming more due to having an increased fan total pressure ratio. As previously explained in the result section, the cruise-only design's fan power is almost equal to its total power consumed.

The remaining power draw is due to the weight drag. Across both designs, the heat exchanger and duct are the two heaviest components in the system and therefore increase the power draw the most.

## 5. Discussion and conclusion

In this work, the ram-air cooling system for a regional fuel cell aircraft has been designed and evaluated using an optimization-based method. Two optimal designs were presented, a realistic dual-point design capable of take-off operation, and an idealized cruise-only design. The dual-point results indicate that it is possible, even with conservative technology assumptions (Table A.1), to satisfy the heat rejection requirement of an ATR 72-sized fuel cell aircraft and do so with reasonable stack power usage. This result is only attainable with a significant thrust generation and we identify three key enablers to this: inlet oversizing, an application-suited heat exchanger design and a front-mounted fan.

The use of inlet oversizing for cruise has been reported in previous studies [21,22] due to the take-off constraint. While oversizing is beneficial from an internal flow standpoint, it is on the other hand increasing the external drag. It was therefore thought that the use of a fan would have the effect of limiting this oversizing, since it is able to both increase the mass flow at take-off and decrease the heat exchanger entry Mach number during cruise, without increasing the diameter of the installation. This has not been the case in this study. Instead, every design optimization performed has resulted in a design that during cruise achieves a near full recovery of the dynamic pressure upstream of the inlet. The limit to this oversizing was identified to be the onset of inlet spillage drag. Consequently, the optimizer steered the designs to reduce the critical mass flow ratio for spillage drag. Having the highest static pressure possible when entering the heat exchanger, even when an upstream fan is present, results in minimal losses and presents the most favorable conditions for thrust generation.

The selection of a heat exchanger design for the application, namely fuel cell aircraft heat rejection, is reflected in the heat exchanger non-dimensional parameters: the void fraction ratio, $\sigma_r$, the surface area density ratio, $\alpha_r$, and the solidity factor, $\chi$. The prioritization of low heat exchanger entry Mach numbers shifts the heat exchanger design space towards geometries with relatively low compactness, owing to large air-side frontal areas. The optimal void fraction ratio, surface area density ratio and solidity factor for the dual-point design were found to be around 25.4, 6.4 and 0.035, respectively. A heat exchanger of this geometry can be described as being very open on the air side while still maintaining a large heat transfer area. This means that a large amount of heat can be transferred without increasing the air's speed excessively, minimizing frictional losses. The required increase in heat transfer during take-off is then delivered by running a higher coolant mass flow, which is "cheap" from a system power draw perspective.

For the location of the fan, the upstream and downstream locations perform very similarly in the mission-weighted total power draw, and no clear winner can be identified based on this performance parameter. There are however some clear advantages to using the front-mounted fan. The first major advantage over the rear fan is the reduced air speed and external pressure losses over the heat exchanger, which is a result of the compression done by the fan. The second advantage compared to the rear fan is the reduction in required shaft power when operating upstream of the heat exchanger, as compressing colder air requires less work. The rear fan, however, has the advantage of not increasing the heat exchanger inlet temperature, which is reflected in lower required mass flows. Nevertheless, this rear fan advantage is marginal at these fan specifications and is expected to reduce with increased fan efficiency. We do however realize that the low air mass flows requirement in these oversized designs make the front fan designs advantageous, as the required compression work in take-off is not that high. Setting a restrictive maximum diameter constraint on the cooling duct might therefore turn the tide in favor of the rear fan designs.

Ultimately, the results of this study indicate that it is possible to provide the required cooling for regional fuel cell aircraft operating with 80 °C low temperature PEMFC systems. If the fuel cell is only expected to operate during cruise, then a rather compact ram-air cooling system can be implemented, using only around 4.3 % of an expected total stack power output of 1.2 MW. In order to extend the operation to include an ISA +25 °C hot-day take-off, a larger system is required, which is expected to increase the cooling system's power consumption during cruise to around 11.3 % of the total stack output. In take-off, 15.2 % is consumed out of the expected 2 MW total stack power output.

## CRediT authorship contribution statement

**Christian Svensson:** Writing – original draft, Software, Methodology, Conceptualization; **Petter Miltén:** Methodology; **Tomas Grönstedt:** Writing – original draft, Conceptualization.

## Declaration of competing interest

The authors declare that they have no known competing financial interests or personal relationships that could have appeared to influence the work reported in this paper.

## Acknowledgments

The Competence Center TechForH2 is hosted by Chalmers University of Technology and is financially supported by the Swedish Energy Agency (P2021-90268) and the member companies Volvo, Scania, Siemens Energy, GKN Aerospace, PowerCell, Oxeon, RISE, Stena Rederierier AB, Johnsson Matthey and Insplorion.

## Data availability

Data will be made available on request.

## Appendix A. Supplementary modeling and calculation details

### A.1. Fixed model parameters

### A.2. Duct station calculations

The inlet ingests a mass flow $\dot{m}_{\text{air}}$, which sets the captured streamtube area in the freestream

$$A_\infty = \frac{\dot{m}_{\text{air}}}{v_\infty \rho_\infty}$$

which then sets the area-ratio between the streamtube area at the farfield station ∞ and the intake face at station 0, which is the inverse of the commonly known mass flow-ratio parameter (MFR)

$$\text{AR}_\infty = 1/\text{MFR} = A_1/A_\infty \,.$$

The streamtube experiences isentropic ($\pi = \tau = 1$) subsonic compression, if MFR < 1, or expansion, if MFR > 1, before entering the cooling duct inlet. The flow then enters the inlet and is between station 1 and station 2 subject to subsonic diffusion by means of a diffuser with area-ratio $\text{AR}_d$ and divergence half-angle $\theta_d$. The flow experiences a loss of total pressure inside the diffuser, via a total pressure ratio $\pi_d$

$$p_{02} = p_{01} \cdot \pi_d \,.$$

In the presence of a booster fan, the air between station 2 and station 3 is subjected to polytropic compression with an efficiency $\eta_{\text{fan}}$. Otherwise, the air remains unchanged. The fan total pressure ratio $\pi_{\text{fan}}$ is a state variable and is changed by the solver to satisfy the cooling mass flow need

$$p_{03} = \begin{cases} p_{02} \\ p_{02} \cdot \pi_{\text{fan}} \quad \text{(if fan)} \end{cases}$$

$$T_{03} = \begin{cases} T_{02} \\ T_{02} \left(\pi_{\text{fan}}\right)^{\frac{\gamma-1}{\eta_{\text{fan}} \cdot \gamma}} \quad \text{(if fan)} \,. \end{cases}$$

**Table A.1**
Fixed parameters for aircraft, heat exchanger, cooling duct, fan, and pump systems.

| Parameter | Value | Description |
|---|---|---|
| *Aircraft* | | |
| $\eta_{\text{prop}}$ | 80 % | Propulsive efficiency |
| $\eta_{\text{motor}}$ | 95 % | Motor efficiency |
| $T_{\text{FC}}$ | 353.15 K | Fuel cell stack temperature |
| *Heat Exchanger* | | |
| Coolant | Water-Ethylene glycol mix (50-50) | "Zitrec M" in CoolProp [33] |
| $t_w$ | 0.5 mm | Wall/plate thickness |
| $t_f$ | 0.15 mm | Fin thickness |
| $\ell_{\text{air}}$ | 6.12 mm | Undisturbed flow length, air |
| $\ell_{\text{coolant}}$ | 6.12 mm | Undisturbed flow length, coolant |
| $\ell/\sqrt{t_f}$ | 0.5 $\text{m}^{1/2}$ | Fin characteristic dimension |
| $\rho_{\text{HEX}}$ | 2730 kg/$\text{m}^3$ | Material density (Al 3003) |
| $k_{\text{HEX}}$ | 185 W/(m · K) | Thermal conductivity (Al 3003) |
| *Cooling Duct* | | |
| $L_{2\text{–}3}/d_3$ | 0.1 | Axial length to diameter ratio |
| $L_{4\text{–}5}/d_3$ | 0.1 | Axial length to diameter ratio |
| $L_{5\text{–}6}/d_3$ | 1.0 | Axial length to diameter ratio |
| $m/A_{\text{duct}}$ | 3 kg/$\text{m}^2$ | Cooling duct areal density |
| *Fan* | | |
| $\eta_{\text{fan}}$ | 80 % | Fan polytropic efficiency |
| $\eta_{\text{motor, fan}}$ | 98 % | Fan motor efficiency |
| $P/m_{\text{fan}}$ | 2000 W/kg | Fan + motor assembly specific power |
| *Pump* | | |
| $\eta_{\text{pump}}$ | 60 % | Pump efficiency |
| $P/m_{\text{pump}}$ | 450 W/kg | Pump specific power |

The downstream Mach number is then found by considering a constant area duct. Between station 3 and station 4 the air is heated inside the heat exchanger and loses total pressure due to heat addition and friction. The air-side downstream conditions are solved using a compressible formulation for flow through a constant-area duct with both friction and heat addition [34], with the left-hand side friction factor being calculated using GenHEX (see Section 2.6). The coolant-side pressure drop is calculated using the incompressible formulation found in [26]. The coolant mass flow is determined by the heat to be dissipated, the desired temperature drop $\Delta T_{\text{coolant}}$ and the coolant specific heat capacity

$$\dot{m}_{\text{coolant}} = \frac{Q_{\text{req.}}}{c_{p,\,\text{coolant}}\Delta T_{\text{coolant}}}\,.$$

The heat exchanger coolant inlet temperature is assumed to be that of the fuel cell stack operating temperature, i.e. $T_{\text{h, in}} \approx T_{\text{FC}}$. In the same manner as the previous constant area section, a booster fan can be put between station 4 and station 5 to increase the total pressure

$$p_{05} = \begin{cases} p_{04} \\ p_{04} \cdot \pi_{\text{fan}} \quad \text{(if fan)} \end{cases}$$

$$T_{05} = \begin{cases} T_{04} \\ T_{04}\left(\pi_{\text{fan}}\right)^{\frac{\gamma-1}{\eta_{\text{fan}}\cdot\gamma}} \quad \text{(if fan)}\,. \end{cases}$$

Between station 5 and station 6, the air goes through a variable convergent nozzle, before exiting the duct into the freestream. The nozzle is considered isentropic and by that

$$p_{06} = p_{05}\,.$$

### A.2.1. Inlet total pressure loss

The total pressure ratio $\pi_d$ in the cooling duct inlet is a function of the throat Mach number $M_1$, the area-ratio $\text{AR}_d$ and the diffuser half-angle $\theta$, and utilizes the `ESDU 80037` correlation method [35]. It describes the total pressure ratio over the intake as

$$\pi_d = 1 - \Delta\pi_l - \Delta\pi_{\text{cs}} - \Delta\pi_{\text{d}} N$$

where $\Delta\pi_l$ is the loss increment caused by the lip geometry and inlet mass flow ratio MFR, $\Delta\pi_{\text{cs}}$ loss increment caused by constant area sections before and after the diffuser, $N$ a "magnifying factor" which represents interaction between the lip losses and diffuser performance, and $\Delta\pi_{\text{d}}$ the loss increment from the diffuser itself.

## A.3. Component power calculation

The power draw for the coolant pump is calculated as

$$P_{\text{pump}} = \frac{\dot{m}_{\text{coolant}}\Delta p_{0,\,\text{coolant}}}{\rho_{\text{coolant}}\eta_{\text{pump}}}\,,$$

where $\Delta p_{0,\,\text{coolant}}$ is the change in coolant total pressure across the HEX and $\rho_{\text{coolant}}$ is the liquid coolant density. For the booster fan stage, the power consumed is the shaft power with an electric effiency $\eta_{\text{motor, fan}}$

$$P_{\text{fan}} = \frac{\dot{m}_{\text{air}} c_{p_{\text{air}}} \Delta T_{0,\,\text{fan}}}{\eta_{\text{fan, motor}}}\,,$$

where $\Delta T_{0,\,\text{fan}}$ is the change in total temperature across the fan stage.

## A.4. Component mass calculation

The heat exchanger mass is calculated as

$$m_{\text{HEX}} = V_t \cdot \chi \cdot \rho_{\text{HEX}}\,,$$

where $\rho_{\text{HEX}}$ is the density of the material used in the heat exchanger (see Table A.1). The coolant mass considered is the one corresponding to the coolant volume inside the heat exchanger

$$m_{\text{coolant}} = (\rho\sigma)_{\text{coolant}} V_t\,.$$

The mass of the cooling duct is calculated as

$$m_{\text{duct}} = m/A_{\text{duct}} A_{\text{duct}}\,,$$

where $m/A_{\text{duct}}$ is the material areal density (see Table A.1) and $A_{\text{duct}}$ the combined wetted area of the internal and external surfaces. The pump and fan masses are calculated using a specific power value and the max device power used (usually during take-off)

$$m_{\text{pump}} = \frac{P_{\text{pump, max}}}{P/m_{\text{pump}}}$$

$$m_{\text{fan}} = \frac{P_{\text{fan, max}}}{{}^{P}/_{m_{\text{fan}}}}.$$

## Appendix B. Accuracy of code

The accuracy of the quasi-1D approach has been assessed by comparing it to a 2D axisymmetric RANS simulation performed using the commercial CFD solver STAR-CCM+. The coupled solver is used with the ideal gas formulation and the SST $k-\omega$ turbulence model together with a low $y^+$ approach. The domain is a hemisphere of $r = 50\,\text{m}$ and its farfield was set to the freestream boundary condition. A single design, $A_0 = 1\,\text{m}^2$, $\text{AR}_d = 1.4$, $L_x = 0.35\,\text{m}$ was used throughout the assessment. The geometry was generated using the method described in Section 2.7.1. No heat exchanger or fan stage was modeled. The internal flow was instead subjected to a constant total heat source inside the heat exchanger region (this was replicated in the quasi-1D code by applying Rayleigh flow between station 3 and station 4). The total force acting on the cooling duct ("Net force") is calculated as

$$\text{Net force} = F_{\text{cowl}} + F_{\text{inlet}} - F_{\text{gross}}\,. \tag{B.1}$$

Here, $F_{\text{cowl}}$ is the pressure and shear forces acting in the axial direction on the outer wetted area $S_{\text{wet,out}}$

$$F_{\text{cowl}} = \int_{S_{\text{wet, out}}} (p - p_\infty) + \tau_x \,\mathrm{d}A\,,$$

where $p$ is the local static pressure and $\tau_x$ the wall-shear stress acting in the axial direction. The terms $F_{\text{inlet}}$ (the ram and additive drag) and $F_{\text{gross}}$ are the pressure and momentum forces acting on the inlet and exit planes, respectively

$$F_{\text{inlet}} = \int_{A_0} \rho v_x^2 + (p - p_\infty)\,\mathrm{d}A\,,$$

$$F_{\text{gross}} = \int_{A_6} \rho v_x^2 + (p - p_\infty)\,\mathrm{d}A\,,$$

where $\rho$ is the local density and $v_x$ the local air speed in the axial direction. The net force from the CFD simulations (Eq. B.1) is equivalent to the sum $D_{\text{ext}} + D_{\text{int}}$ from the quasi-1D code (Eqs. 10 and 12).

First, the grid convergence of the 2D axisymmetric RANS simulation was assessed through the *grid convergence index* (GCI). Two integral quantities are considered, the net force on the geometry and the mass flow through the duct. The mesh base size was decreased in multiples of two, resulting in cell counts of 158286, 420011, and 1237294 for the coarse, medium, and fine grid, respectively. The resulting average cell size refinement ratio was then 1.629 from coarse to medium and 1.716 from medium to fine. The GCI results are summarized in Table B.1. The medium refinement level was shown to be satisfactory, and was therefore used for the rest of the CFD study.

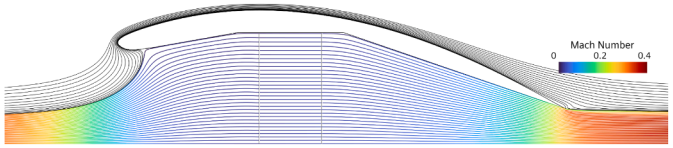


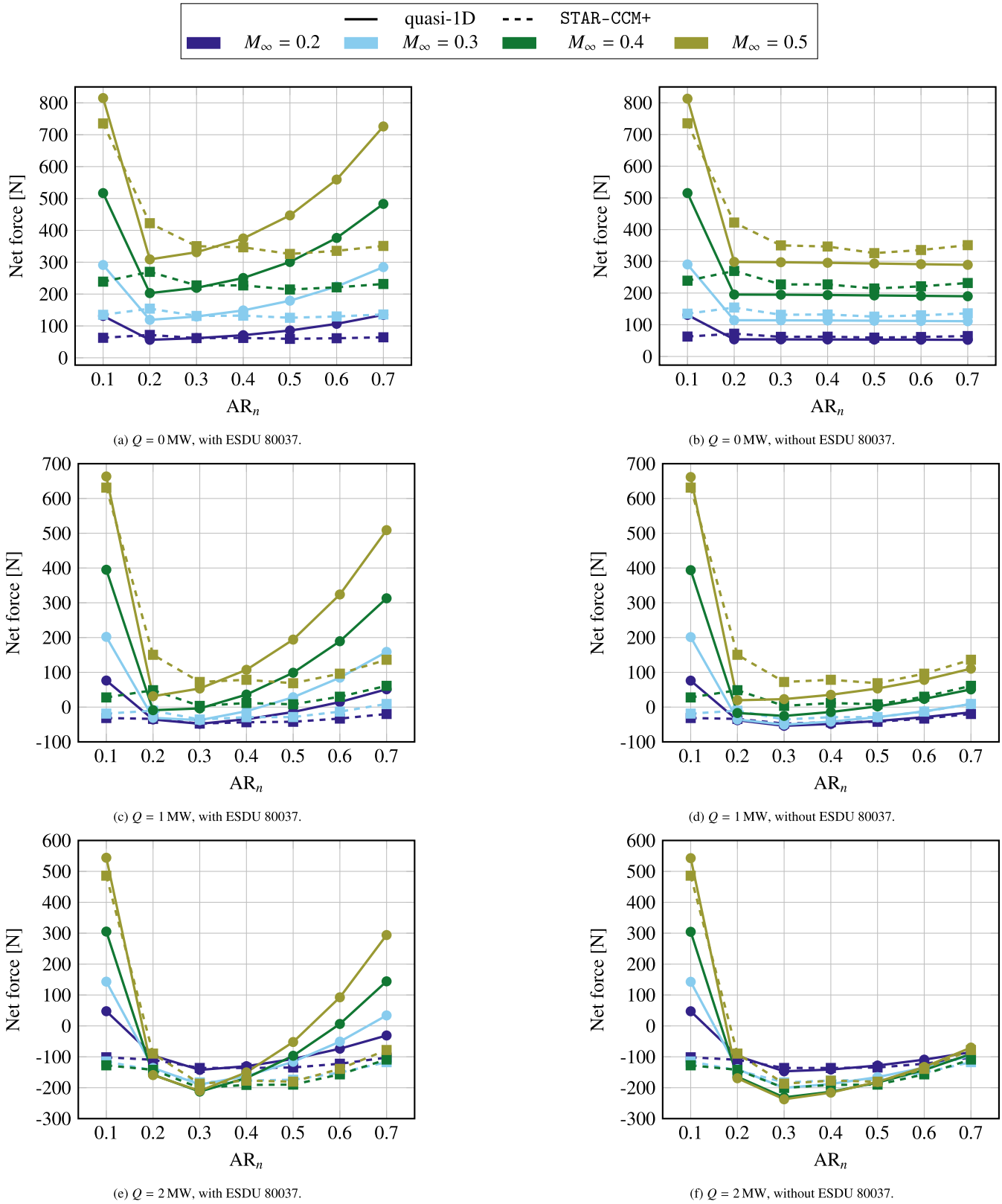

**Fig. B.1.** Streamline plot from STAR-CCM+ of the simulated geometry. Captured streamtube is indicated by the Mach-colored streamlines. $M_\infty = 0.4$, $Q = 1\,\text{MW}$, $\text{AR}_n = 0.1$.

The cooling duct design was then simulated at different nozzle area ratios, Mach numbers and levels of heat addition. The atmospheric conditions were set to ISA conditions at 6400 m. The simulation sweep is then repeated in the quasi-1D code. This was done both with and without the ESDU 80037 method for inlet loss, as it was noticed that the method would overpredict the internal drag by a great amount at higher area nozzle ratios, see Fig. B.2. A reason for this could be an elevated throat Mach number then leads the ESDU 80037 method to predict an aggressive rise in internal losses. In the quasi-1D code, the stagnation point of the streamtube boundary is always assumed to be at the inlet highlight (station 0). However, in reality and as was seen in the CFD, the streamtube boundary will instead stagnate on the internal geometry (see Fig. B.1), which will result in a lessened flow acceleration. At $\text{AR}_n = 0.1$, the ESDU 81024 external drag method greatly overpredicts the spillage drag for all Mach numbers except at $M_\infty = 0.5$, where it slightly overpredicts. The general overprediction of the spillage drag is consistent with the findings in [36]. The large spillage drag increase seen in the CFD at $M_\infty = 0.5$ is likely due to a shock-induced separation on the external lip surface.

It should also be noted that, regardless of inlet losses, that the mass flow is overpredicted by the quasi-1D model as it assumes an ideal perfectly expanded nozzle. In reality, and as is observed in the CFD simulations, the static pressure at the nozzle exit is not equal to the ambient, due to streamline curvature effects and viscous losses internally and externally.

**Table B.1**
Summary of grid convergence study performed at three different freestream Mach numbers. $\phi$ is the quantity of interest, GCI the grid convergence index, $\text{GCI}_a$ the asymptotic value (where a value close to unity indicates convergence), and $\mathcal{P}$ the achieved simulation order.

| | | Net force | | | | Mass flow air | | | |
|---|---|---|---|---|---|---|---|---|---|
| $M_\infty$ | Grid | $\phi$ | GCI | $\text{GCI}_a$ | $\mathcal{P}$ | $\phi$ | GCI | $\text{GCI}_a$ | $\mathcal{P}$ |
| 0.2 | Coarse | 59.546 N | - | 0.995 | 2.035 | 10.051 kg/s | - | | |
| | Medium | 58.830 N | 0.895 % | | | 10.117 kg/s | 0.778 % | 1.003 | 1.471 |
| | Fine | 58.549 N | 0.299 % | | | 10.151 kg/s | 0.350 % | | |
| 0.4 | Coarse | 219.812 N | - | 0.994 | 2.079 | 20.343 kg/s | - | | |
| | Medium | 216.628 N | 1.045 % | | | 20.479 kg/s | 0.766 % | 1.003 | 1.507 |
| | Fine | 215.406 N | 0.342 % | | | 20.549 kg/s | 0.338 % | | |
| 0.6 | Coarse | 500.313 N | - | 0.993 | 1.986 | 31.357 kg/s | - | | |
| | Medium | 491.366 N | 1.412 % | | | 31.625 kg/s | 0.757 % | 1.004 | 1.793 |
| | Fine | 487.734 N | 0.491 % | | | 31.744 kg/s | 0.286 % | | |




(a) $Q = 0$ MW, with ESDU 80037.

(b) $Q = 0$ MW, without ESDU 80037.

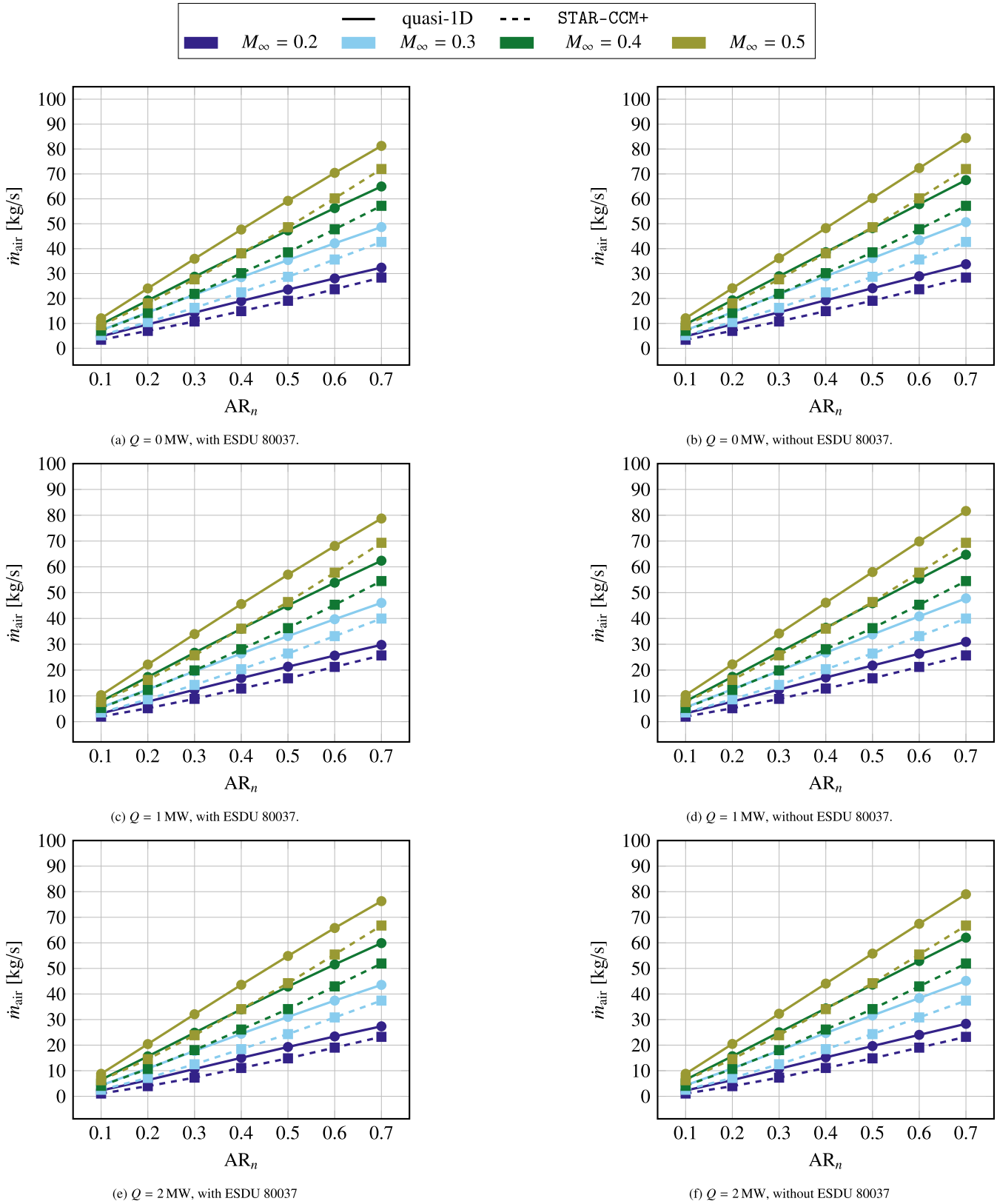
(c) $Q = 1$ MW, with ESDU 80037.

(d) $Q = 1$ MW, without ESDU 80037.

(e) $Q = 2$ MW, with ESDU 80037.

(f) $Q = 2$ MW, without ESDU 80037.

**Fig. B.2.** Comparison of net force between quasi-1D and 2D axisymmetric (STAR-CCM+). Pure heat addition without a heat exchanger. $A_0 = 1\,\text{m}^2$, $\text{AR}_d = 1.4$, $L_x = 0.35\,\text{m}$.




(a) $Q = 0$ MW, with ESDU 80037.

(b) $Q = 0$ MW, without ESDU 80037.

(c) $Q = 1$ MW, with ESDU 80037.

(d) $Q = 1$ MW, without ESDU 80037.

(e) $Q = 2$ MW, with ESDU 80037

(f) $Q = 2$ MW, without ESDU 80037

**Fig. B.3.** Comparison of mass flow between quasi-1D and 2D axisymmetric (STAR-CCM+). Pure heat addition without a heat exchanger. $A_0 = 1\,\text{m}^2$, $\text{AR}_d = 1.4$, $L_x = 0.35$ m.

## References


[1] Airbus, First ZEROe engine fuel cell successfully powers on, 2024, (Airbus Newsroom). Accessed: 2026-05-18, https://www.airbus.com/en/newsroom/stories/2024-01-first-zeroe-engine-fuel-cell-successfully-powers-on

[2] H.J. van Gerner, T. Luten, W. Resende, G. Mühlthaler, M.-B. Buntz, System analysis and comparison between a 2 MW conventional liquid cooling system and a novel two-phase cooling system for fuel cell-powered aircraft 18 (4) 849. https://doi.org/10.3390/en18040849

[3] A.B. de Vasconcelos Leitão, C. Bringhenti, J.T. Tomita, F.J. dos Santos Silva, C. Xisto, T. Grönstedt, A review of hydrogen aircraft propulsion systems: recent advances and environmental perspectives, Int. J. Hydrog. Energy 176 (2025) 151489. https://doi.org/10.1016/j.ijhydene.2025.151489

[4] A.C. Frey, D. Bosak, E. Madrid, J. Stonham, C.M. Sangan, O.J. Pountney, Thermal management in high temperature proton exchange membrane fuel cells for aircraft propulsion systems, Prog. Aerosp. Sci. 153 (2025) 101052. On Pathways to Green Aviation, https://doi.org/10.1016/j.paerosci.2024.101052

[5] F.W. Meredith, Cooling of Aircraft Engines with Special Reference to Ethylene Glycol Radiators Enclosed in Ducts, Aeronautical Research Committee Reports & Memoranda ARC/R&M-1683, H. M. Stationery Office, 1935. https://reports.aerade.cranfield.ac.uk/handle/1826.2/1425

[6] N. Sciences, Aircraft gas turbine engines, in: Commercial Aircraft Propulsion and Energy Systems Research: Reducing Global Carbon Emissions, The National Academies Press, Washington, D.C., 2016, p. 37. https://doi.org/10.17226/23490

[7] M. Schröder, F. Becker, C. Gentner, Optimal design of proton exchange membrane fuel cell systems for regional aircraft, Energy Convers. Manage. 308 (2024) 118338. https://doi.org/10.1016/j.enconman.2024.118338

[8] L. Braumann, C. Gross, A. Juen, H. Amri, Achieving Hot-Day Take-Off with Fuel Cells Through Efficient Thermal Management, Technical Report, exFan project, 2024. https://exfan-project.eu/sites/default/files/ADT_DLRK2024.pdf

[9] J.F. Hellmuth, P.R. Menke, A.G. von Schweinitz, P. Koschel, W. Tegethoff, M. Heere, C. Thomas, J. Köhler, Novel two-phase based cooling systems for fuel cell electric aircraft, Appl. Therm. Eng. 280 (2025) 127275. https://doi.org/10.1016/j.applthermaleng.2025.127275

[10] F. Quaium, T. Bielsky, F. Thielecke, Fuel cell cooling system design for hydrogen-powered concept aircraft 10 pages. https://doi.org/10.25967/570127

[11] C.K. Sain, J. Hänsel, S. Kazula, Conceptual design of air and thermal management in a nacelle-integrated fuel cell system for an electric regional aircraft, in: AIAA Aviation Forum 2023, AIAA.

[12] V. Habrard, V. Pommier-Budinger, I. Hazyuk, J. Jézégou, E. Benard, Parametric study of a liquid cooling thermal management system for hybrid fuel cell aircraft 12 (5) 377. https://doi.org/10.3390/aerospace12050377

[13] M. Nozinski, P. Meyer, F. Delony, J. Friedrichs, J. Göing, S. Kabelac, On the design and operation of the thermal management system of PEMFC-powered aircraft 13 (3) 243. https://doi.org/10.3390/aerospace13030243

[14] M. Niehuis, P. Jeschke, Performance calculation of the thermal management system for a fuel cell aircraft engine, J. Glob. Power Propuls. Soc. 10 (2026) 29–49. https://doi.org/10.33737/jgpps/213543

[15] T.L. Kösters, X. Liu, D. Kožulović, S. Wang, J. Friedrichs, X. Gao, Comparison of phase-change-heat-pump cooling and liquid cooling for PEM fuel cells for MW-level aviation propulsion 47 (68) 29399–29412. https://doi.org/10.1016/j.ijhydene.2022.06.235

[16] R. Ahluwalia, X. Wang, A. Shah, M.G. Lauer, P.J. Ansell, Fuel cells for single-aisle regional aircraft: system configuration, performance and cost, Int. J. Hydrog. Energy 159 (2025) 150568. https://doi.org/10.1016/j.ijhydene.2025.150568

[17] M. Wiegand, L. Schuchard, S.D. Lauro, M. Lange, R. Mailach, Fuel cell hybrid-electric aircraft performance: optimizing thermal management for reduced climate impact, Volume 1: Aircraft Engine; Ceramics and Ceramic Composites of *Turbo Expo*, ASME, 2025, p. V001T01A004. https://doi.org/10.1115/GT2025-151328

[18] A.C. Frey, J. Stonham, D. Bosak, C.M. Sangan, O.J. Pountney, Radiators in fuel cell powered aircraft: the effect of heat rejection on drag, Appl. Therm. Eng. 274 (2025) 126697. https://doi.org/10.1016/j.applthermaleng.2025.126697

[19] A.C. Frey, D. Bosak, J. Stonham, C.M. Sangan, O.J. Pountney, Liquid cooling of fuel cell powered aircraft: the effect of coolants on thermal management, J. Eng. Gas Turbines Power 146 (11) (2024) 111021. https://doi.org/10.1115/1.4066047

[20] F. Armbrüster, R. Schaber, P. Pöchhacker, J. Schroeter, J. Friedrichs, Design exploration of a ram-air-based heat exchanger system for disruptive engines, Aeronaut. J. 129 (1341) (2025) 3142–3164. https://doi.org/10.1017/aer.2025.10045

[21] E.J. Adler, A.H.R. Lamkin, J.R.R.A. Martins, Aircraft ducted heat exchanger aerodynamic shape and thermal optimization, ASME J. Heat Mass Transf. 147 (1) (2024) 011902. https://doi.org/10.1115/1.4066438

[22] H. Kellermann, M. Lüdemann, M. Pohl, M. Hornung, Design and optimization of ram air–based thermal management systems for hybrid-electric aircraft, Aerospace 8 (1) (2021). https://doi.org/10.3390/aerospace8010003

[23] F.P. Incropera, D.P. Dewitt, T.L. Bergman, A.S. Lavine, Incropera's Principles of Heat and Mass Transfer, John Wiley & Sons, 2017.

[24] P. Miltén, I. Jonsson, A. Lundbladh, C. Xisto, Generalized method for the conceptual design of compact heat exchangers, J. Eng. Gas Turbines Power 146 (11) (2024) 111018. https://doi.org/10.1115/1.4065922

[25] P. Miltén, I. Jonsson, A. Lundbladh, M. Wiegand, C. Xisto, Estimating the performance of application-suited heat exchangers, in: Proceedings of ASME Turbo Expo 2026: Turbomachinery Technical Conference and Exposition, GT2026, American Society of Mechanical Engineers, Milan, Italy, 2026. Paper No. GT2026-176739.

[26] W.M. Kays, A.L. London, Compact Heat Exchangers, Krieger Publishing Company, 1998.

[27] ESDU, Drag of Axisymmetric Cowls at Zero Incidence for Subsonic Mach Numbers, Technical Report 81024, ESDU.

[28] A. Petrusson, Aerodynamic Evaluation of Nacelles for Engines with Ultra High Bypass Ratio, Master's thesis, 2017. https://odr.chalmers.se/items/dcc21be5-3292-4e41-bda7-adb0384fe429

[29] J. Gabler, Optimagic: a library for nonlinear optimization, 2022. https://github.com/optimagic-dev/optimagic

[30] T.H. Rowan, Functional stability analysis of numerical algorithms, 1990. https://api.semanticscholar.org/CorpusID:117559971

[31] S.G. Johnson, The NLopt nonlinear-optimization package, 2007, (https://github.com/stevengj/nlopt)

[32] C. Svensson, A.A.M. Oliveira, T. Grönstedt, Hydrogen fuel cell aircraft for the Nordic market, Int. J. Hydrog. Energy 61 (2024) 650–663. https://doi.org/10.1016/j.ijhydene.2024.02.382

[33] I.H. Bell, J. Wronski, S. Quoilin, V. Lemort, Pure and pseudo-pure fluid thermophysical property evaluation and the open-source thermophysical property library CoolProp, Ind. Eng. Chem. Res. 53 (6) (2014) 2498–2508. https://doi.org/10.1021/ie4033999

[34] J.I. Sturas, An exact closed-form solution for constant-area compressible flow with friction and heat transfer, NASA, 1971, Technical Report NASA TN D-6566.

[35] ESDU, Pressure recovery of axisymmetric intakes at subsonic speeds, ESDU, Technical Report 80037.

[36] A. Heidebrecht, T. Stańkowski, D. MacManus, Parametric geometry and CFD process for turbofan nacelles, Proceedings of the ASME Turbo Expo 2016: Turbomachinery Technical Conference and Exposition, American Society of Mechanical Engineers, Seoul, South Korea, 2016. https://doi.org/10.1115/GT2016-57784